Bioactive Materials 49 (2025) 1–22

Contents lists available at ScienceDirect

Bioactive Materials

journal homepage: www.keaipublishing.com/en/journals/bioactive-materials

Piezoelectric nanofilms fabricated by coaxial electrospun polycaprolactone/Barium titanate promote Achilles tendon regeneration by reducing IL-17A/NF-κB-mediated inflammation

Wufei Dai [a,e,1], Qi Xu [a,c,1], Qinglin Li [b], Xiansong Wang [a], Wenjie Zhang [a], Guangdong Zhou [a], Xu Chen [d,*], Wei Liu [a,**], Wenbo Wang [a,***]

[a] Department of Plastic and Reconstructive Surgery, Shanghai Key Laboratory of Tissue Engineering, Shanghai Ninth People's Hospital, Shanghai Jiao Tong University School of Medicine, Shanghai, 200011, China
[b] Department of Aesthetic Surgery, Zhumadian Central Hospital, Zhumadian, 463000, China
[c] Department of Surgery, Air Force Medical Center, PLA, Beijing, 100142, China
[d] Department of Laboratory Medicine, Shanghai Ninth People's Hospital, Shanghai Jiao Tong University School of Medicine, Shanghai, 200011, China
[e] Department of Medicine 1, University Hospital Erlangen, Friedrich-Alexander University Erlangen Nuremberg, Erlangen, Germany

ARTICLE INFO

Keywords:
Achilles tendon regeneration
Piezoelectric PCL/BTO nanofilm
Macrophage and T cells
Immunomodulation
IL-17A/NF-κB signaling pathway

ABSTRACT

Tendon injuries are often exacerbated by persistent inflammation, which hampers tissue regeneration. In this study, we developed a noninvasive, wirelessly controlled, and self-powered piezoelectric nanofilm fabricated by coaxial electrospinning of polycaprolactone (PCL) and tetragonal barium titanate nanoparticles (BTO), and investigated its roles in modulating inflammation and repairing Achilles tendon defects as well as the mechanism in a rat model. *In vitro* study and *in vivo* study upon subcutaneous implantation showed that the piezoelectric PCL/BTO nanofilms could inhibit M1 macrophage polarization and reduce the secretion of inflammatory factors. Moreover, when bridging an Achilles tendon defect, the nanofilms could promote tenogenic gene expression including collagen deposition, and collagen remodeling, facilitate functional tendon recovery and significantly reduce tissue inflammation by suppressing M1 macrophage polarization and promoting M2 polarization. Moreover, the piezoelectric stimulation could also enhance tendon regeneration by inhibiting angiogenesis, reducing lipid deposition, and decreasing ectopic ossification. Mechanistically, the piezoelectric nanofilms reduced tissue inflammation mainly via inhibiting the nuclear factor (NF)-κB signaling pathway that is mediated by interleukin (IL)-17A secreted from $CD3^+$ T cells, and thus to reduce proinflammatory factors, such as IL-1β and IL-6, inducible nitric oxide synthase, monocyte chemoattractant protein-1, and tumor necrosis factor-α. These findings indicate the potential of piezoelectric stimulation in immunomodulation, and in promoting tendon regeneration via IL-17A/NF-κB-mediated pathway.

1. Introduction

The Achilles tendon endures significant force by connecting the calf muscles to the heel bone and thus enables leg movement. It is highly prone to injury with poor self-repair and regenerative capacity. This often leads to prolonged recovery, complications, and reduced life quality for millions [1,2]. Following tendon injury and defects, inflammation is an inevitable phase of the healing response that initiates the

Peer review under the responsibility of KeAi Communications Co., Ltd.

* Corresponding author. Department of Laboratory Medicine, Shanghai Ninth People's Hospital, Shanghai Jiao Tong University School of Medicine, 639 Zhi Zao Ju Road, Shanghai, 200011, China.
** Corresponding author. Department of Plastic and Reconstructive Surgery, Shanghai Key Laboratory of Tissue Engineering, Shanghai Ninth People's Hospital, Shanghai Jiao Tong University School of Medicine, China.
*** Corresponding author. Department of Plastic and Reconstructive Surgery, Shanghai Key Laboratory of Tissue Engineering, Shanghai Ninth People's Hospital, Shanghai Jiao Tong University School of Medicine, China.
E-mail addresses: chenxu917@shsmu.edu.cn (X. Chen), liuwei_2000@yahoo.com (W. Liu), wangwenbo0903@126.com (W. Wang).
[1] These authors contributed equally to this study.

https://doi.org/10.1016/j.bioactmat.2025.02.038
Received 1 December 2024; Received in revised form 22 February 2025; Accepted 25 February 2025
Available online 1 March 2025

tendon repair process. The persistent inflammation, characterized by the excessive accumulation of macrophages and T cells, along with elevated levels of proinflammatory factors such as interleukin-1β (IL-1β), IL-6, IL-17A, tumor necrosis factor-α (TNF-α), and inducible nitric oxide synthase (iNOS), has a significant negative impact on tendon regeneration [3,4].

While proinflammatory factors aid in clearing necrotic tissue fragments and cells, their excessive production can cause apoptosis of healthy cells, prolong inflammation and repair time and thus hinder the recovery process [5,6]. Research has shown that persistent inflammation can reduce collagen content in joint ligaments, disrupt collagen microstructure, and result in irregular collagen fiber structure and abnormal diameter distribution, leading to significantly reduced mechanical properties [7]. In addition, chronic inflammation can increase collagen III/I ratio, further decreasing the collagen fibril diameter [8,9]. Macrophage secreted collagenase degrades collagen, and mast cell phagocytosis of collagen also impacts collagen remodeling [10]. This phenomenon may culminate in the accumulation of fibrotic scar tissue, compromising the mechanical integrity of the repaired tendon, thus heightening the susceptibility to reinjury [11]. Therefore, effective inflammation management is crucial for promoting optimal tendon regeneration.

The use of bioactive scaffold materials to modulate the inflammatory response plays a crucial role in tendon regeneration [12]. However, biomaterial implantation inevitably triggers an inflammatory response [13]. If the implanted material is difficult to degrade, an extended period of M1 macrophage polarization can lead to an increase in M2 macrophages, which in turn promotes the secretion of fibrotic factors and the formation of fibrous encapsulation around the implant. Additionally, macrophages may fuse to each other to form foreign body giant

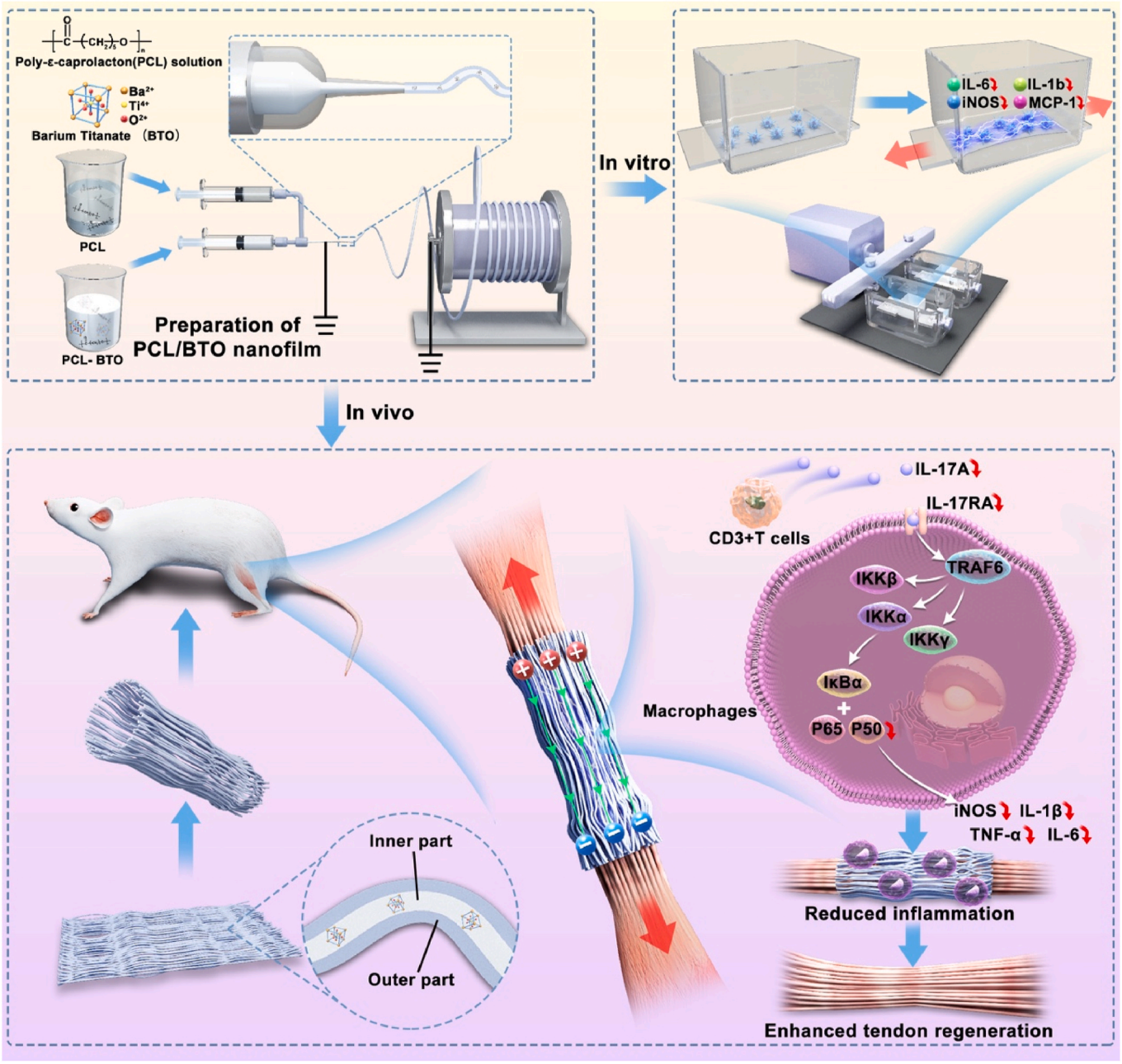

Scheme. A novel piezoelectric PCL/BTO nanofilm prepared by coaxial electrospinning is employed to accelerate of tendon regeneration via alleviating inflammation through the inhibition of IL17A/NF-κB signaling pathway.

cells, which often persist around the material and hinder tissue integration by secreting more inflammatory factors. This process can recruit other immune cells, such as mast cells, basophils, and T lymphocytes, exacerbating chronic inflammation, and therefore further reinforce the fibrous encapsulation and potentially leading to ectopic ossification [14–16].

Previous studies have reported that applying local electric fields or currents could influence inflammatory responses [17,18]. Successfully integrating electrical stimulation with synthetic materials can offer a novel approach for developing tendon regenerative scaffolds by modulating the inflammatory microenvironment at the implantation site. When implanted in the body, piezoelectric polymer materials do not require an external power source; instead, they generate electrical stimulation through material deformation caused by body's natural movements (such as squeezing or pulling), leading to charge changes and the bioelectric effect. Piezoelectric tissues in the body include bone, cartilage, tendons, ligaments, and skin [19]. There have been reports on the ability of piezoelectric biomimetic materials to promote stem cell differentiation and facilitate the regeneration of bone, cartilage, tendons, and nerve tissues [20–22]. Wu *et al.* have reported a conductive hydrogel that generated electrical stimulation *in situ*, promoted neural stem cell differentiation and accelerated axon regeneration [23]. However, the effect of piezoelectric stimulation on immune cells and the related mechanisms in tendon repair remain unclear.

In this study, piezoelectric polycaprolactone (PCL) was selected due to its suitable mechanical properties and biocompatibility, and piezoelectric tetragonal BaTiO3 nanoparticles (BTO) were incorporated into PCL by coaxial electrospinning to develop a wireless piezoelectric stimulation system. Subsequently, the nanofilms were characterized and their biocompatibility was evaluated. Additionally, the anti-inflammatory or tendon regeneration activities of the nanofilms were also investigated respectively *in vitro* and *in vivo* using a rat implantation model (Scheme 1).

Upon mechanical activation, the triggered piezoelectric potential can inhibit the inflammatory response by reducing macrophage production of proinflammatory cytokines, particularly by reducing IL-17A secretion, and inhibiting IL-17A/nuclear factor (NF)-κB signaling pathway. Additionally, the piezoelectric stimulation of PCL/BTO can also inhibit inflammation-induced excessive vascularization and promote collagen deposition, maturation, and orderly arrangement, thus to promote tendon repair.

2. Results and discussion

2.1. Characterization for piezoelectric properties of PCL and PCL/BTO nanofilms

Two types of nanofilms, PCL and PCL/BTO, were designed and fabricated using the coaxial electrospinning technology. As shown in Fig. 1a and b, PCL and PCL/BTO nanofilms exhibit flexible white films with ordered nanofibers when observed with scanning electron microscope (SEM), which reveals similar diameters of 0.93 ± 0.13 (PCL) and 0.92 ± 0.14 μm (PCL/BTO) between two groups. The transmission electron microscopy (TEM) with elemental mapping shows the distribution of carbon, oxygen, barium, and titanium in fibers (Fig. 1c). Additionally, BTO nanoparticles were evenly distributed in the core of the nanofibers using the coaxial electrospinning technology. As shown in Fig. 1l and m, similar to the SEM results, the nanofibers of PCL and PCL/BTO nanofilms are ordered and have similar diameters. The contents of barium and titanium elements in the PCL/BTO nanofilm are 6.13 % and 2.11 % respectively quantified by inductively coupled plasma mass spectrometry (Fig. 1d). Thus, successful integration of BTO powder into PCL and the formed PCL/BTO nanofilms are confirmed, and this approach was specifically selected to encapsulate piezoelectric BTO nanoparticles into PCL in order to prevent direct cell contact with the piezoelectric compound.

As shown in Fig. 1e, X-ray diffractometer (XRD) characterization reveals typical two curves. After removing the background noise, no characteristic diffraction peaks were observed in the XRD pattern of PCL nanofilms (bottom curve). In contrast, the XRD pattern of PCL/BTO nanofilms (top curve) exhibits six distinct diffraction peaks corresponding to BTO, with reflection peaks at 2θ values associated with the (100), (110), (111), (200), (210), and (211) planes. These peaks resulted in clear reflections in the XRD image, which is consistent with the noncentrosymmetric structure of the tetragonal phase of BTO. Piezoelectric compounds exhibit piezoelectric properties only in specific structural phases. For example, the cubic phase of barium titanate is nonpiezoelectric, while its tetragonal phase, owing to its asymmetry, possesses piezoelectric characteristics.

Piezoresponse force microscopy (PFM) was used to investigate the piezoelectric properties of PCL and PCL/BTO nanofilms. The piezoelectric response amplitude and phase curves can be used to confirm the piezoelectricity of the PCL/BTO nanofilm. As shown, the phase angle of PCL nanofilms fail to be reversed by 180° under a direct current bias (Fig. 1f), and they did not exhibit typical butterfly curve (Fig. 1h), indicating an absence of piezoelectricity. By contrast, the phase angle is reversed by 180° under a direct current bias (Fig. 1g), and a complete butterfly curve is observed (Fig. 1i), confirming the piezoelectric properties of PCL/BTO. To further investigate the piezoelectric function, the output external voltage of the PCL/BTO nanofilms was measured with mechanical stretching models at specific frequencies. As shown in Fig. 1j, very little output voltage is detected from the PCL nanofilm under the same conditions. By contrast, PCL/BTO nanofilms generate an increasing output voltage (2, 5, and 10 V) as the $BaTiO_3$ concentration increased (3.33 %, 6.67 %, and 10 %) (Fig. 1k).

However, higher concentrations of $BaTiO_3$ would lead to agglomeration of the nanoparticles, negatively impacting both the mechanical properties and piezoelectric performance of the composite. Increasing the concentration beyond 10 % did not significantly improve the piezoelectric output. In fact, the agglomeration compromised the mechanical properties of the scaffold.

As shown in Fig. S1, to further verify the optimal concentration, we prepared 2D films where $BaTiO_3$ nanoparticles (5 %, 10 %, and 20 %, w/v) were mixed with PDMS and polarized to evaluate the piezoelectric performance and the biological effects. The results indicated that while a 20 % $BaTiO_3$ concentration did not further enhance piezoelectric performance, the 10 % concentration generated the highest voltage output. When macrophages were seeded on these films and exposed to mechanical strain, the 10 % $BaTiO_3$ group exhibited optimal effect on modulating inflammatory factor production. Notably, the 20 % $BaTiO_3$ group showed effects on macrophages similar to that of the 10 % group, suggesting no additional benefit from the higher concentration. Therefore, we selected the 10 % concentration of $BaTiO_3$ for all subsequent material characterizations, *in vitro* experiments, and *in vivo* studies.

Derjaguin–Muller–Toporov (DMT) modulus can be used to quantify the elasticity of the material, which is the ability to return to its original shape after being stressed. DMT modulus images of the two nanofilms were obtained using atomic force microscopy (AFM), followed by frequency distribution diagrams of the DMT modulus (Fig. 1n, o, p and q). Statistical analysis revealed that the DMT modulus of PCL/BTO was 7.91 ± 0.95 MPa, compared with 3.64 ± 0.41 MPa for PCL, indicating better elasticity for PCL/BTO (Fig. 1r). Additionally, Fig. 1s shows changes in roughness, which can be attributed to incorporating BTO nanoparticles.

The mechanical properties of PCL and PCL/BTO nanofilms were investigated using a universal testing machine. As shown in Fig. 2a–d, after incorporating BTO nanoparticles, the PCL/BTO nanofilms exhibit improved mechanical properties, with a higher tensile strength, Young's modulus, and maximum load, measured at 24.66 ± 1.02 MPa, 49.59 ± 2.90 MPa, and 32.60 ± 2.78 N, respectively. The pure PCL nanofilms have corresponding values of 17.81 ± 0.85 MPa, 40.93 ± 3.75 MPa, and 22.56 ± 3.97 N. Additionally, the strain at break for the PCL/BTO nanofilms (37.83 % ± 3.77 %) is lower than that of PCL nanofilms

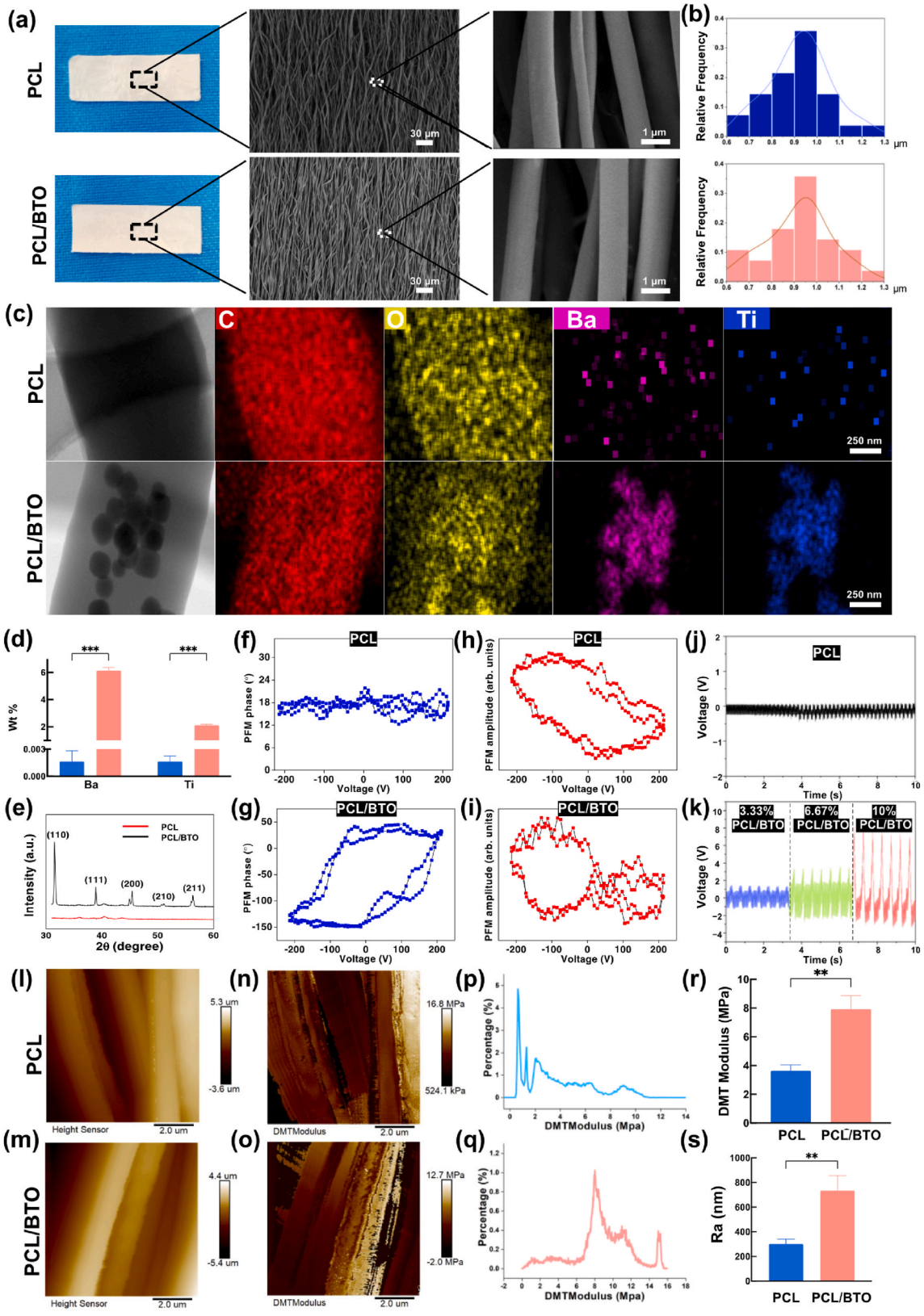

Fig. 1. Characterization for piezoelectric properties of PCL and PCL/BTO nanofilms. (a) Gross view and SEM image of PCL and PCL/BTO nanofilms. Bars = 30 μm and 1 μm. (b) Diameter frequency distribution statistics of PCL and PCL/BTO nanofilms. (c) The corresponding elemental mapping images of PCL and PCL/BTO nanofilms by TEM. Bar = 250 nm. (d) ICP–MS test of two nanofilms. (e) XRD pattern of two nanofilms. (f) & (g) Piezoresponsive force microscopy (PFM) phase of PCL and PCL/BTO nanofilms. (h) & (i) PFM amplitude of PCL and PCL/BTO nanofilms. (j) & (k) The output voltage of PCL and PCL/BTO nanofilms under 4 % stretching tension at 2 Hz. (l) & (m) Topography image of PCL and PCL/BTO nanofilms. (n) & (o) DMT modulus image of PCL and PCL/BTO nanofilms. (p) & (q) DMT modulus frequency distribution statistics of PCL and PCL/BTO nanofilms. (r) DMT modulus of two nanofilms. (s) Roughness of two nanofilms. $^{**}p < 0.01$ and $^{***}p < 0.001$.

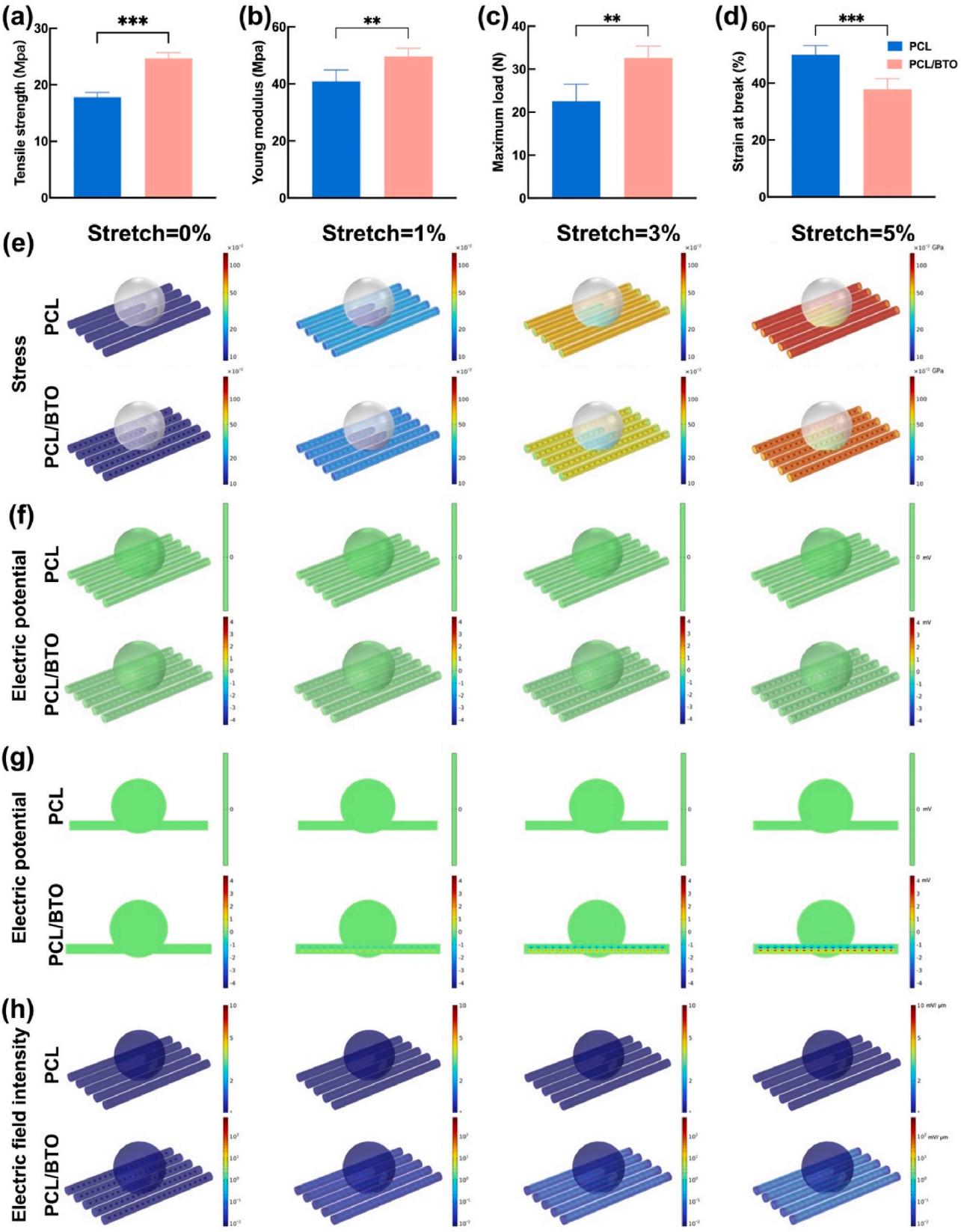

Fig. 2. PCL/BTO nanofilm has good mechanical properties, and finite element analysis shows the electric field and potential generated under 0 %, 1 %, 3 %, and 5 % stretch. (a) Tensile strength; (b) Young's modulus; (c) maximum load; (d) strain at break of two nanofilms; (e) Stress. (f) & (g) electric potential; (h) electric field intensity. $^{**}p < 0.01$, $^{***}p < 0.001$.

(50.05 % ± 3.14 %). These results indicate that PCL/BTO nanofilms can withstand higher tensile forces while undergoing less deformation, making them a promising material for tendon tissue engineering.

Finite element analysis was conducted to simulate the electric potential and electric field produced by the two nanofilms under 0 %, 1 %, 3 %, and 5 % deformation. As shown in Fig. 2e, the stress in both nanofilms increased with deformation without breaking. For PCL/BTO, as deformation increased from 0 % to 5 %, the electric field and potential also increased from 0 mV/μm and 0 V to12.13 mV/μm and 4.40 mV, respectively (Fig. 2f–h, S2a, and S2b). In contrast, the PCL nanofilm dose not generate any electric potential or field, regardless of the deformation levels, which is in consistence with the PFM results.

2.2. Piezoelectric PCL/BTO nanofilms demonstrate improved biocompatibility and exhibit enhanced anti-inflammatory properties

To verify the piezoelectric effects on macrophages, we placed the nanofilms (1 × 3 cm^2) in a bioreactor to undergo mechanical stimulation (Fig. 3a). As shown in Fig. 3b, F-actin staining shows that after 24 h of stretching, macrophages on PCL nanofilms remain round, while those on PCL/BTO nanofilms adapte a spindle shape, a morphological characteristic of anti-inflammatory M2 macrophages [24]. To investigate the biocompatibility of PCL and PCL/BTO nanofilms, macrophages and tenocytes were cultured on nanofilms with or without mechanical stimulation for one and three days respectively. As shown in Fig. S3, using cell counting kit-8 (CCK-8), the viability of macrophages on both PCL and PCL/BTO nanofilms, whether subjected to mechanical stimulation or not, is similar among different groups. This indicates that neither PCL nor PCL/BTO nanofilms exhibited significant cytotoxicity, which is consistent with previous reports [25,26]. PCL is a biodegradable polymer widely employed in various biomedical fields. It has been approved by both the FDA (Food and Drug Administration) and the CE (Conformité Européenne) marking for the use in numerous medical devices and drug delivery systems since the 1980s (i.e. Capronor®, SynBiosys®, Monocryl®suture) [26]. The degradation of $BaTiO_3$ (BTO) within the material results in the release of Ba^{2+} ions, a naturally occurring element in the human body, though typically found only in trace amounts in bone tissue. Many studies have demonstrated the successful incorporation of BTO into PCL for *in vivo* tissue regeneration, further confirming the biocompatibility and potential of these materials for tissue engineering applications [27,28]. For tenocytes (Fig. 3c), although there is no significant difference in the viability of each group on the first day, there was a significant increase in the viability of stretched tenocytes (PCL-ST and PCL/BTO-ST) on the third day compared with the viability of the non-stretched groups (PCL-S and PCL/BTO-S), indicating that stretch can promote the proliferation of tenocytes, which is in consistence with the previous studies [29].

Additionally, SEM examination demonstrates that macrophages adhere tightly to PCL and PCL/BTO nanofilms (Fig. 3d). In the different groups, macrophages cultured statically on PCL nanofilms (PCL-S) were used as the control group. As shown, in the static state, there is no significant difference in the expression of inflammatory factors between PCL and PCL/BTO nanofilms (Fig. 3e). Also shown in Fig. S4, under static conditions, PCL/BTO materials with different BTO concentrations fail to induce a significant immune reaction. This suggests that without mechanical stimulation, BTO materials do not markedly influence macrophage mediated inflammation, and the piezoelectric response induced by mechanical stimulation is the key factor for activating its biological effects.

Compared with the control (PCL-S), the PCL-ST group shows a significant increase in the expression of inflammatory factors, except for *CD206*, which aligns with the previous reports showing that mechanical stimulation promotes inflammatory responses [30]. In contrast, macrophages in the PCL/BTO-ST group shows a significant reduction of the gene expression of proinflammatory factors (Fig. 3e). In addition, there is no significant difference in the expression of anti-inflammatory factors (*IL-10* and *arginase-1*) between the two groups subjected to stretching, suggesting that mechanical stimulation promotes the expression of inflammatory factors, which is unfavorable for tissue repair. However, piezoelectric stimulation can revert this effect, and significantly reduce the production of proinflammatory factors, thereby mitigating inflammation and fostering a pro-repair immune microenvironment.

Mechanical stimulation is an essential component of the tendon development microenvironment. However, after tendon injury, excessive mechanical loading can lead to increased production of inflammatory factors, which can disrupt the local immune microenvironment, negatively impacting tendon regeneration [31]. Studies have shown that mechanical loading induced the secretion of proinflammatory factors through the Piezo1 or Yes-associated protein signaling pathway, causing indirect damage [32,33]. Excessive inflammation during tendon regeneration can lead to several adverse outcomes, including tendon fibrosis and heterotopic ossification [34,35].

Previous studies have reported that externally applied local electric fields or currents could promote macrophage migration and reduce the expression of inflammatory factors such as *IL-1*, *TNF-α*, and *IL-18* [36]. Additionally, a study has shown that ultrasound-induced piezoelectric stimulation could promote M1 macrophage polarization [37]. However, in our experiment (Fig. 3), piezoelectric stimulation generated through tensile strain could reduce M1 polarization and inhibit the gene expression of inflammatory factors, while promote M2 macrophage polarization. This difference may be attributed to the variations in material structure and the type of mechanical stimulus that drove material deformation. Moreover, Liu *et al.* have found that a piezoelectric hydrogel used for treating periodontitis induced osteogenic differentiation of stem cells in the inflammatory periodontal ligament and reshaped an anti-inflammatory and pro-regenerative niche by switching M1 to M2 macrophage phenotype [38]. This is consistent with our *in vitro* results (Fig. 3).

The *in vivo* biocompatibility and piezoelectric-induced inflammatory changes of PCL and PCL/BTO nanofilms were further investigated by subcutaneously implanting 1 × 1 cm^2 nanofilms in Sprague Dawley rats (Fig. 4a). As shown, at day 14 and 28 postsurgery, hematoxylin and eosin (H&E) staining shows that the PCL nanofilms have greater inflammatory cell infiltration, indicating more pronounced inflammation, while the PCL/BTO group exhibits less inflammatory cell infiltration and a thinner fibrous capsule around the material (Fig. 4b). The depth of cell infiltration in PCL vs PCL/BTO-ST is respectively 179.87 ± 28.85 μm vs 84.03 ± 8.85 μm at day 14 and is respectively 430.78 ± 33.02 μm vs 139.88 ± 53.77 μm at day 28 (Fig. S5).

Additionally, the productions of proinflammatory factors (iNOS and IL-6) are reduced in the PCL/BTO group, whereas the productions of anti-inflammatory factors (CD206 and IL-10) are increased (Fig. 4c–j). These findings suggest that PCL/BTO nanofilms can reduce local inflammation and create an anti-inflammatory immune microenvironment. This is consistent with our *in vitro* findings (Fig. 3), indicating that the deformation of the aligned piezoelectric material can modulate the inflammatory microenvironment in the tissue. The piezoelectric effect is generated because deformed abdomen by natural movements of the rats, such as eating, breathing, muscle contractions and general activity. This, in turn, leads to deformation of the subcutaneously implanted material, resulting in electrical stimulation.

2.3. Piezoelectric PCL/BTO nanofilms promote collagen deposition, Achilles tendon regeneration, and functional recovery of the tendon

To evaluate the effect of PCL and PCL/BTO nanofilms on tendon regeneration, we constructed a 0.6-cm Achilles tendon defects model in the hind limbs of rats(Fig. 5a). The PCL nanofilms were implanted in the left hind limb, while the PCL/BTO nanofilms were implanted in the right hind limb. To assess functional recovery of the Achilles tendon, gait experiment was conducted at days 14, 28, and 56 post-surgery, to analyze four parameters: paw area, stride time, swing duration, and

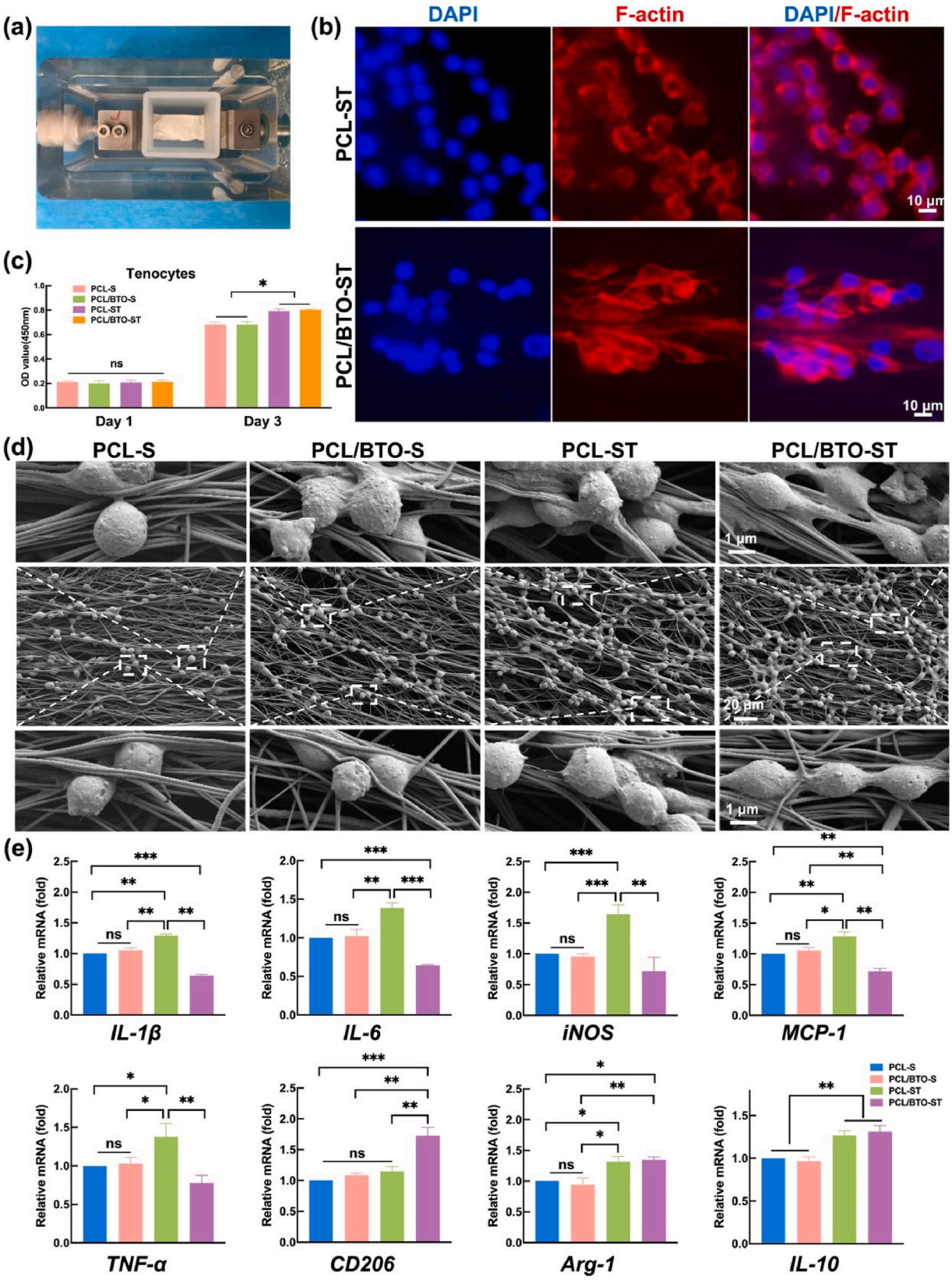

Fig. 3. PCL/BTO nanofilm has good biocompatibility and can decrease inflammatory factor production in macrophages *in vitro*. (a) Nanofilms in a bioreactor. (b) Phalloidin staining of macrophages being stretched on nanofilms. Bar = 10 μm. (c) CCK-8 assay of tenocytes cultured on two nanofilms. (d) SEM images of macrophages cultured on two nanofilms with/without stretch. Top and bottom panels represents selected and enlarged images of cultured cells. Bars = 1 μm and 20 μm. (e) RT-qPCR detection of proinflammatory factors (*IL-1β*, *IL-6*, *iNOS*, *MCP-1*, and *TNF-α*) and anti-inflammatory factors (*CD206*, *Arg-1*, and *IL-10*) in macrophages under piezoelectric stimulation by mechanical stretch. *$p < 0.05$, **$p < 0.01$ and ***$p < 0.001$.

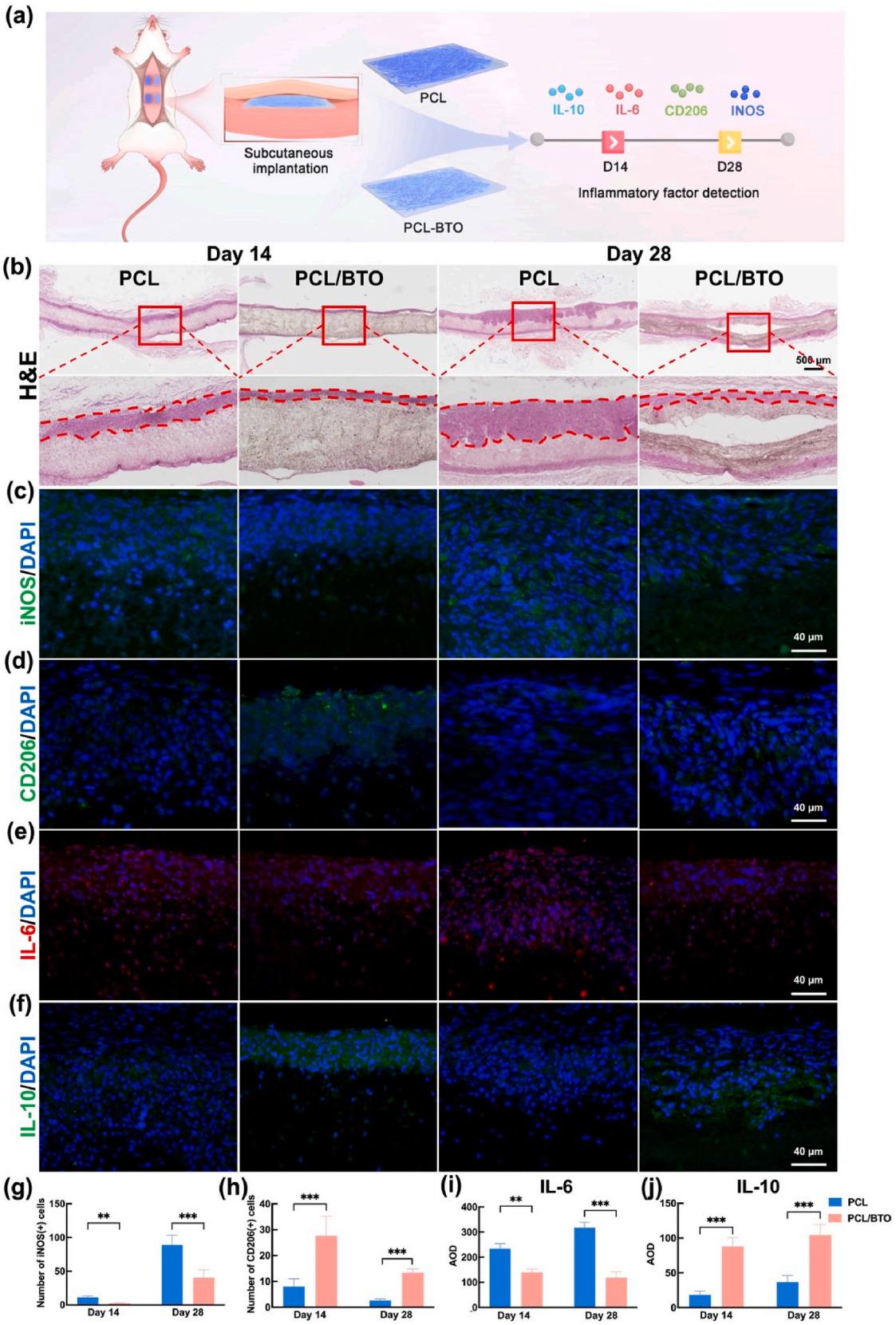

Fig. 4. Subcutaneous implantation experiment demonstrates good biocompatibility and inflammation reduction effect of PCL/BTO nanofilm. (a) Schematic design for nanofilm subcutaneous implantation experiment. (b) H&E staining of nanofilms at days 14 and 28 post-subcutaneous implantation (bar = 500 μm). Immunofluorescent staining of iNOS (c), CD206(d), IL-6(e), and IL-10(f) of nanofilms (bar = 40 μm) and their corresponding semi-quantitative analysis (g–j) at days 14 and 28 post-subcutaneous implantation. $^{**}p < 0.01$ and $^{***}p < 0.001$.

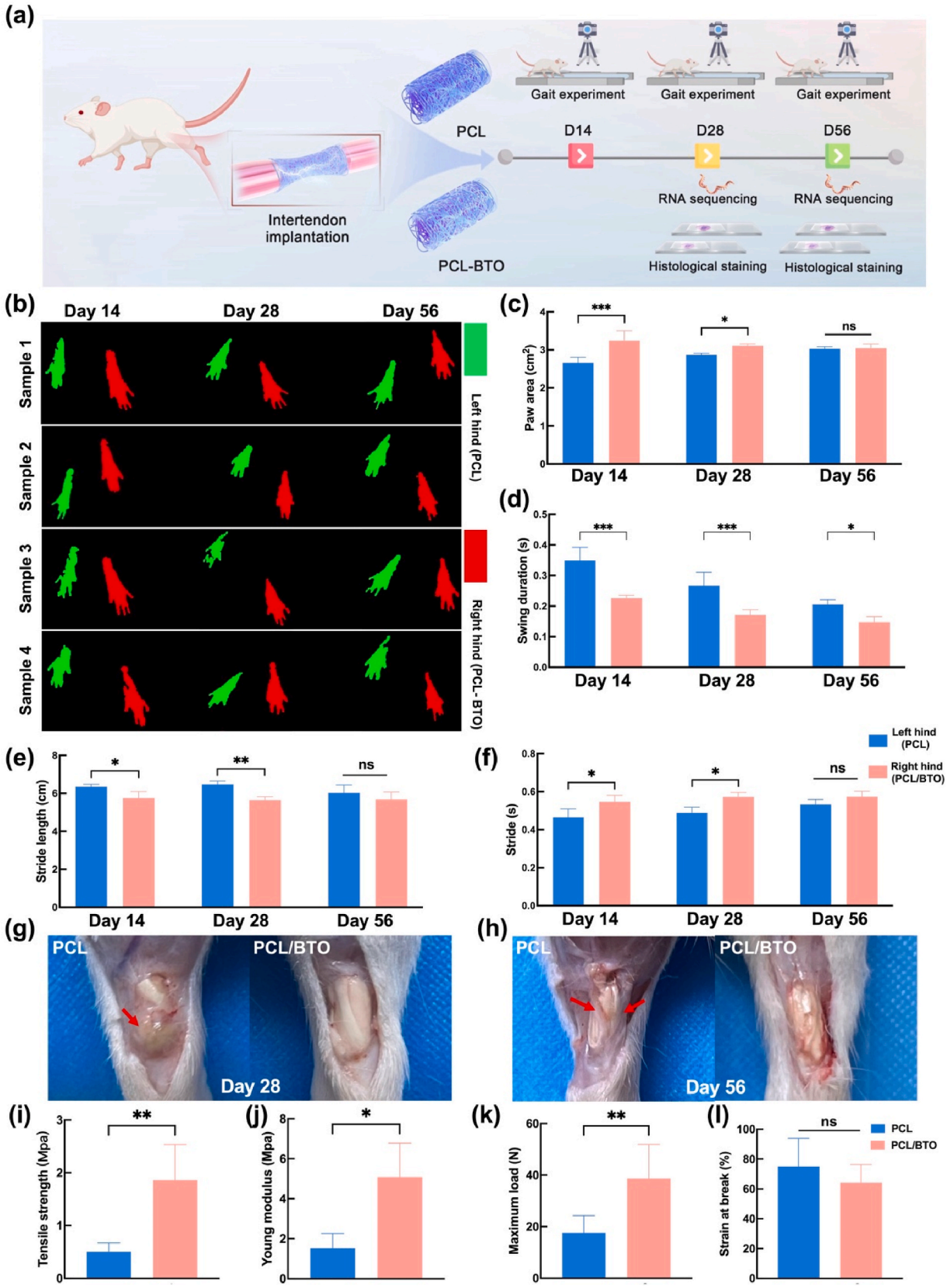

Fig. 5. PCL/BTO facilitates Achilles tendon function recovery and improves the mechanical properties of regenerated tendon tissues. (a) Schematic design of Achilles tendon repair experiment. (b) The gait analysis in coronal planes. Quantitative analysis of spatiotemporal parameters ($n = 4$ rats per group), including paw area (c), swing duration(d), stride length swing time(f),and stride time(e). Gross view of regenerated Achilles tendons treated with PCL and PCL/BTO at day 28 post-operation (g), and treated with PCL and PCL/BTO at day 56 post-operation (h). Mechanical property analyses of regenerated Achilles tendons at day 56 post-operation: Tensile strength (i), Young's modulus (j), Maximum load (k), and Strain at break (l). $*p < 0.05$, $**p < 0.01$ and $***p < 0.001$.

stride length.

Paw area represents the pain and disfunction, the more pain and disfunction, the less paw area. As shown in Fig. 5b and c, at days 14 and 28 post-operation, the paw area of the PCL/BTO group is larger than that of the PCL group with statistical significance ($p < 0.05$), but the difference becomes non-significant at day 56 between two groups ($p > 0.05$), indicating relatively severer pain, disfunction and altered weight-bearing in the PCL group at early phases comparing to BTO group that healed better, but it was relieved at later stage of day 56.

Swing duration is the time during which the foot does not contact the ground. As shown in Fig. 5d, it is relatively shorter in the PCL/BTO group than in the PCL group at days 14, 28 and 56 post-operation, indicating better functional recovery of the repaired Achilles tendon. In contrast, prolonged swing duration in the PCL group may indicate discomfort or impaired functionality of PCL repaired tendon.

Stride length is the measured distance between consecutive placements of the same foot on the ground, and reflects the compensatory response to discomfort or pain of affected foot, the shorter the more discomfort. As shown in Fig. 5e,the stride length is significantly shorter in PCL group than in PCL/BTO group at days 14 and 28 with significant difference ($p < 0.05$), but the difference becomes non-significant at day 56 between two groups ($p > 0.05$).

Stride time is the duration of one complete gait cycle that also reflects foot function. A reduced stride time suggests that the rats need to alter their gaits to minimize weight-bearing on the injured limb, the shorter, the more impaired functionality. As shown in Fig. 5f, the stride time is significantly shorter in PCL group than in PCL/BTO group at days 14 and 28, indicating poorer function in the PCL group. The difference, however, becomes non-significant at day 56 ($p > 0.05$). Likewise, Achilles Functional Index (AFI) values also indicate a better functional recovery in the PCL/BTO group comparing to PCL group with significant differences at days 14, 28 and 56 ($p < 0.05$) (Fig. S6).

At days 28 and 56 post-surgery, regenerated neo-tendon tissues were harvested for mechanical property testing to further evaluate the effectiveness of the treatment. Peritendinous adhesions were assessed using direct visualization of the surgical site of the Achilles tendon. As shown, compared with the PCL group, the tissue around the neo-tendon in the PCL/BTO group appears smoother and can be easily lifted with tweezers showing minimal adhesion (Fig. 5g and h), suggesting reduced inflammation in tendons treated with PCL/BTO nanofilms, particularly at the early stages of repair.

The mechanical analysis shows that the tensile strength, Young's modulus, and maximum load of the PCL/BTO nanofilms–treated tendon are significantly higher than those of the PCL nanofilms–treated group (Fig. 5i–k), suggesting that the neo-tendons in the PCL/BTO group are likely to be more resistant to rupture and capable of withstanding greater forces at day 56 post-operation. We also compared the mechanical properties of PCL/BTO nanofilm-treated tendons with those of normal tendons. According to Fig. S7, except for tensile strength which is higher in normal tendon than in PCL/BTO, there are no significant difference for maximum load, strain break and Young's modulus between PCL/BTO and normal tendons, indicating good functional recovery.

As shown in Fig. 6a and b, at day 28, the fibrils of tendons treated with PCL/BTO nanofilms are denser and have a larger diameter (50.50 ± 5.30 nm) compared with the regenerated tendon fibrils treated with PCL nanofilms (38.08 ± 4.65 nm). At day 56, the diameter of tendon fibrils is increased in both groups, but PCL/BTO group exhibits a more pronounced increase (62.61 ± 4.85 nm) than that of the PCL group (43.80 ± 5.65 nm). Additionally, the PCL group exhibits uneven and sparse fiber distributions, suggesting that piezoelectric stimulation may promote the thickening of tendon fibrils. Tendon fibers are primarily composed of collagen, specifically type I collagen, which mainly provides tensile strength of the tendon [39]. Tendon fibrils with larger diameters typically contain more collagen molecules and higher collagen density, resulting in greater tensile strength. Therefore, the TEM results are consistent with the results of the mechanical property test of regenerated tendon tissue (Fig. 5 and S7).

In Achilles tendon tissue, increased collagen deposition along with reduced inflammation and cell apoptosis can enhance the load-bearing capacity of the tendon while minimizing tendon deformation [40–42]. To evaluate collagen deposition, fiber orientation, and collagen composition in the regenerated tendon, we performed histological staining, including H&E, Masson, and Sirius red stainings. As shown, H&E staining reveals that at day 28, the PCL/BTO-treated tendons exhibit higher content of pink-stained collagen and fewer cells. At day 56 post-surgery, the neo-tendons in the PCL/BTO-treated group display thicker collagen, indicating superior regeneration compared to the PCL group (Fig. 6c).

At day 28, Masson staining reveals that the neo-tendon tissue in the PCL group exhibits less collagen content with a disorganized arrangement, whereas the PCL/BTO group shows greater collagen deposition with a more orderly arrangement and the formation of a wavy structure. At day 56, the neo-tendon tissue in the PCL/BTO group develops much better with a typical wavy structure when compared to the PCL group (Fig. 6d). As shown in Fig. 6g and h, at days 28 and 56, the scores for fiber arrangement and structure in the PCL/BTO group are significantly lower than those in the PCL group, suggesting that the new collagen fibers in the PCL/BTO group are more orderly arranged and structurally closer to that of natural tendon fibers.

During tendon repair, the deposition of newly formed collagen is crucial for restoring the structural integrity and function of the ruptured tendon. Additionally, collagen plays a key role in matrix formation and extracellular matrix (ECM) remodeling, providing structural support and restoring mechanical properties during the regeneration process [43,44]. To specifically distinguish the content of different collagen subtypes, we performed Sirius red staining, where green represents immature type III collagen and red represents mature type I collagen. As shown in Fig. 6e, at day 28, the PCL group exhibits very low collagen content, with no obvious type I collagen present, while the PCL/BTO group shows relatively more collagen, including a small amount of red-stained type I collagen. At day 56, the neo-tendons in the PCL/BTO group have higher collagen content, predominantly type I collagen. In contrast, the tendon tissue of the PCL group displays uneven collagen distribution, with a large amount of immature type III collagen. To further evaluate type I collagen content, we performed immunofluorescence staining on the tendon tissue (Fig. 6f). As shown in Fig. 6i, the neo-tendon tissue in the PCL/BTO group contains relatively more type I collagen at each time point, and from day 28 to day 56, a more significant increase in collagen content was observed in both PCL and PCL/BTO group.

In summary, the implantation of pure PCL materials results in the formation of disorganized collagen structures, immature collagen, and fibrotic scar tissue instead of normal tendon tissue, which compromises the structural integrity and increases the risk of post-repair re-rupture, thereby impairing tendon function. Piezoelectric PCL/BTO nanofilms significantly promotes the tendon repair by enhancing collagen deposition, increasing collagen fibril diameter, and facilitating collagen maturation *in vivo* while also supporting the functional recovery of the tendon. These findings highlight the potential of piezoelectric nanofilms in promoting tendon regeneration, offering a promising therapeutic avenue for tendon tissue engineering.

2.4. Piezoelectric PCL/BTO nanofilms decrease inflammation in vivo

Tendon injuries inevitably trigger inflammatory responses that significantly influence the healing process. Following tissue injuries, immune cells, particularly macrophages, rapidly and extensively infiltrate the injury site, playing a critical role in tissue repair [45]. During the early stage of inflammatory responses, macrophages become activated and polarized into a proinflammatory (M1) phenotype, tasked with removing dead cells and tissue debris. In the later stage of

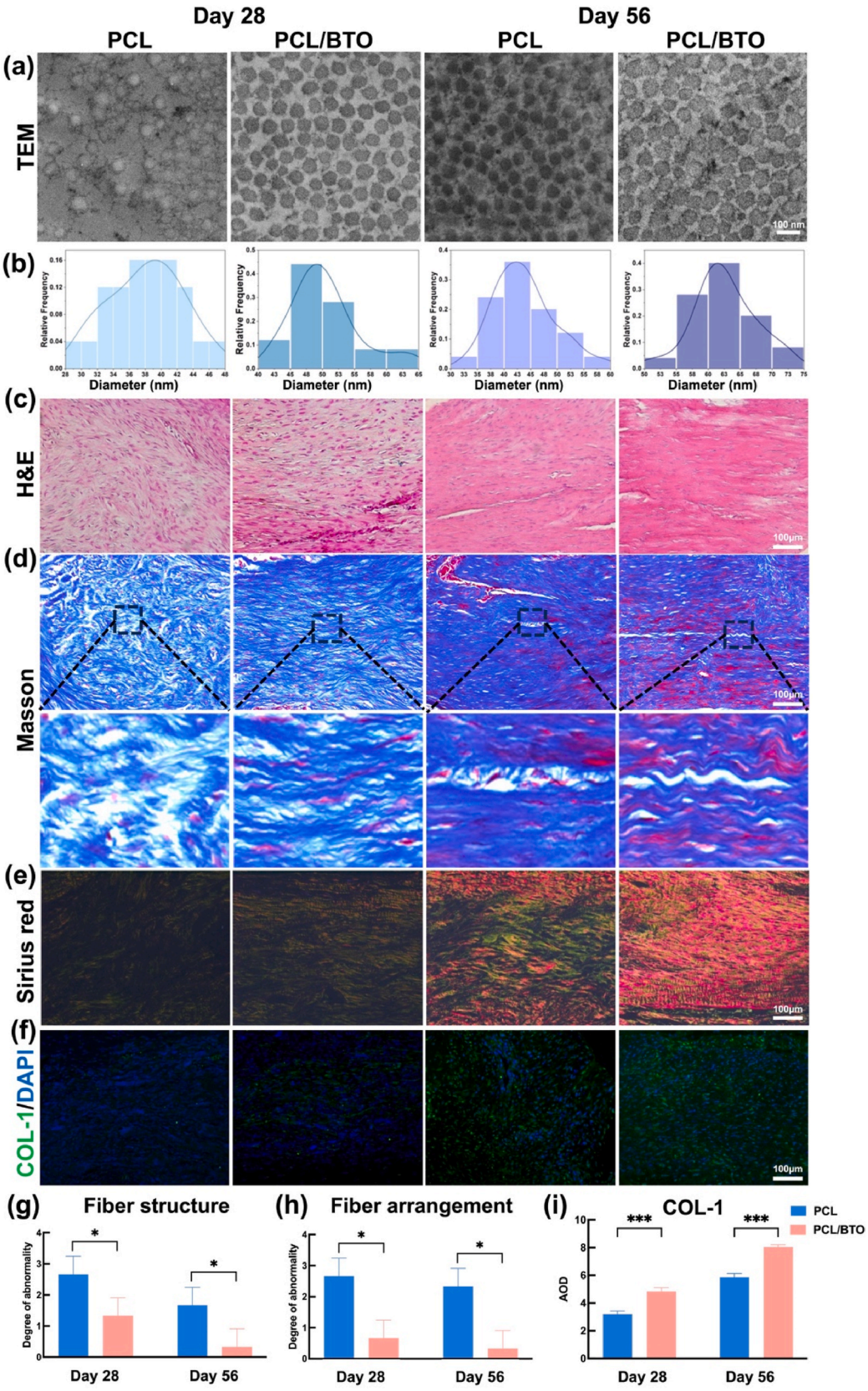

Fig. 6. PCL/BTO nanofilm promotes collagen deposition, maturation, fiber development and arrangement. (a) & (b) TEM image of collagen fibrils in the PCL and PCL/BTO groups at days 28 and 56 post-operation (cross-section view, bar = 100 nm), and their corresponding diameter frequency distribution statistics. (c) H&E staining, (d) Masson staining, (e) Sirius red staining/polarized microscopic image, (f) COL-I immunofluorescent staining of regenerated tendon tissues treated with PCL and PCL/BTO nanofilms at days 28 and 56 post-operation. Bar = 100 μm. (g) Fiber structure scoring analysis. (h) Fiber arrangement scoring analysis. (i) Semi-quantitative analysis of COL-1 staining intensity of regenerated tendon tissues treated with PCL and PCL/BTO nanofilms at days 28 and 56 post-operation. $*p < 0.05$ and $***p < 0.001$.

inflammatory responses, macrophages are prone to switch to the anti-inflammatory (M2) phenotype, which promotes tissue remodeling by stimulating resident cell proliferation and ECM synthesis [46].

The sustained presence of proinflammatory macrophages has been associated with chronic inflammation and tissue injuries. Building on the positive effects of piezoelectric stimulation in reducing proinflammatory factor secretion from macrophages *in vitro*, as well as the results from subcutaneous implantation of piezoelectric materials, we further explored the immunomodulatory and tendon regenerative capacities of the piezoelectric PCL/BTO nanofilms for treating tendon defects *in vivo*.

The gene expression profiles of the PCL and PCL/BTO nanofilm–-treated groups at days 28 and 56 post-operation were comprehensively evaluated using ribonucleic acid (RNA) sequencing. The principal component analysis (PCA) plot reveals that the samples treated with PCL and PCL/BTO nanofilms are well-separated along the first principal component, suggesting that the primary variation in gene expression is driven by piezoelectricity (Fig. S8). Additionally, replicates within the same group shows tight clustering, indicating high reproducibility and consistency within experimental conditions. This analysis focuses on the gene changes related to inflammation, metabolism, and tendon regeneration and on the possible mechanisms by which the piezoelectric stimulation inhibits inflammation *in vivo*.

As shown, at day 28, the heatmap and volcano plot of gene expression (Fig. 7a and b) reveal a total of 818 differentially expressed genes (DEGs) in the PCL/BTO nanofilms–treated group compared with the PCL nanofilms–treated group, with 696 DEGs downregulated. By day 56, 379 DEGs were identified, of which 270 were upregulated (Fig. S9a and b). Fig. S10a displays the top 30 Gene Ontology (GO) terms for differentially expressed genes in the PCL-BTO vs. PCL group at day 28. The differential genes were assigned to three Gene Ontology (GO) categories: biological process (BP), cellular component (CC), and molecular function (MF). GO enrichment analysis at day 28 post-operation reveals that the top 10 downregulated BP include inflammation-related pathways, such as inflammatory response, chemokine-mediated signaling pathway, and neutrophil chemotaxis. Additionally, the top 10 downregulated molecular functions involve several key inflammation-related elements, including chemokine activity, CXCR chemokine receptor binding, and interleukin-1 receptor binding (Fig. 7d and S10b). Most upregulated clusters are related to protein anabolism and sarcomere formation, including ECM, protein binding, and sarcomere (Fig. 7c and S10c). In sharp contrast, at day 56, only CXCR chemokine receptor binding, which is downregulated and related to inflammation, remains among the top 30 clusters. Additionally, several clusters related to muscle contraction, sarcomere formation, myosin filament, and tendon function recovery appear and are upregulated (Fig. S11a-c). At day 56, the up and downregulated GO clusters are similar to those observed at day 28, with many downregulated clusters associated with inflammation and the upregulated clusters associated with tendon regeneration (Fig. 7e and f).

Cytoskeleton is a dynamic network comprising intermediate filaments, microfilaments, and microtubules, which are involved in cell differentiation, migration, adhesion, and mitosis [47]. It has been demonstrated that a strong inflammatory response is the hallmark of the early stage of tendon repair, known as the inflammatory stage. The piezoelectric stimulation generated by the PCL/BTO nanofilms can help reduce inflammation and promote tissue repair. In the later stages, as the inflammatory response diminishes, the ruptured tendon transitions into the repair phase. At this point, the anti-inflammatory, repair-promoting immune microenvironment becomes critical and piezoelectric stimulation can enhance collagen deposition and tendon fiber contraction, thus facilitating tendon regeneration.

To profoundly define the key DEGs, a heatmap of these DEGs related to proinflammatory factors is generated from data of day 28. As displayed in Fig. 7g, the expression of many proinflammatory factor–related genes such as *IL-1β, IL-6, IL-17A*, and *nitric oxide synthase 2* (*iNOS*) are significantly reduced, which implies that PCL/BTO nanofilms is able to assist in building an anti-inflammatory immune microenvironment for tendon regeneration. Then, we performed real-time quantitative reverse transcriptase polymerase chain reaction (RT-qPCR) detection of several proinflammatory factors in the regenerated tendon tissue, including *IL-1β*, *IL-6*, *monocyte chemoattractant protein-1* (*MCP-1*), *iNOS*, and *TNF-α*. As shown in Fig. 7h, the expression of these genes is significantly downregulated in the PCL/BTO group, which is consistent with the results of *in vitro* experiments (Fig. 3). To further evaluate the translation of inflammatory factor genes *in vivo*, we performed immunofluorescence staining of iNOS, CD206, IL-6, and IL-10 on the neotendon tissue at days 28 and 56 post-operation. iNOS-positive macrophages are M1 macrophages (proinflammatory macrophages), which mainly secrete proinflammatory factors such as IL-1β and IL-6. As shown in Fig. 7i, the number of iNOS-positive macrophages is significantly reduced in the PCL/BTO group, along with decreased IL-6 production (Fig. 7k). In contrast, CD206-positive macrophages (anti-inflammatory type) (Fig. 7j) and their secreted IL-10 (Fig. 7l) are significantly increased, demonstrating that the piezoelectric PCL/BTO nanofilms can create an anti-inflammatory microenvironment.

While inflammation is critical for initiating the healing process, excessive or prolonged inflammation can hinder tendon regeneration and lead to chronic conditions, such as tendinopathy. Proinflammatory cytokines such as IL-1β, IL-6, and TNF-α stimulate matrix metalloproteinase expression while inhibit collagen synthesis and deposition, and prolonged inflammation can lead to the release of reactive oxygen species and proteolytic enzymes. This damages ECM components, further weakening tendon integrity and delaying regeneration [48–50]. In this study, piezoelectric stimulation reduced the expression of these proinflammatory cytokines, as confirmed using immunofluorescent staining and transcriptome analysis. Study by Zhang *et al.* reported that reducing inflammation through tendon stem cell exosomes could promote collagen thickening [51]. Our previous study also confirmed that adding hyaluronic acid to the material was able to reduce inflammation and led to increased collagen fiber diameter and the appearance of the characteristic bipolar structure of normal tendons, which was absent in the control group without inflammatory microenvironment modulation [52]. This suggests that piezoelectric stimulation can facilitate collagen remodeling and tendon tissue regeneration by reducing inflammation in the reparative site microenvironment via participating in immune regulation and promoting tissue remodeling.

2.5. *Piezoelectric PCL/BTO nanofilms contribute to tendon repair through multiple metabolic processes*

Tendons are poorly vascularized tissues, and the nutrition is mainly provided by diffusion from synovial fluid instead of blood perfusion [53]. Abnormal angiogenesis can further exacerbate the pathological deposition of ECM, eventually causing scar formation [54]. By enriching angiogenesis-related genes in neo-tendons treated with PCL and PCL/BTO at day 28 post-operation, such as *vascular endothelial growth factor-A* (*VEGF-A*), the expression levels of these genes in the PCL/BTO group are lower than those in the PCL group (Fig. 8a), indicating the antiangiogenic effect mediated by the piezoelectric stimulation. To further verify this effect *in vivo*, immunofluorescence staining of CD31 was performed to observe and quantify the capillaries (Fig. 8d). Angiogenesis was assessed by quantifying the number of capillaries. At days 28 and 56 postsurgery, the number of capillaries in the PCL/BTO group is significantly less than that in the PCL group, with counts of 19 $\pm$ 5.57 vs. 14.67 $\pm$ 3.06 and 28.67 $\pm$ 3.51 vs. 41 $\pm$ 7.81, respectively (Fig. 8e). Simultaneously, less vascularization also represents less blood perfusion, and thus less contribution to the inflammatory cell recruitment, thereby reducing inflammation.

Hypercholesterolemia contributes to persistent cholesterol accumulation inside the immune cells such as macrophages, leading to enhanced inflammation at a tissue repair site. This process is usually caused by activated Toll-like receptors that triggers the upregulation of

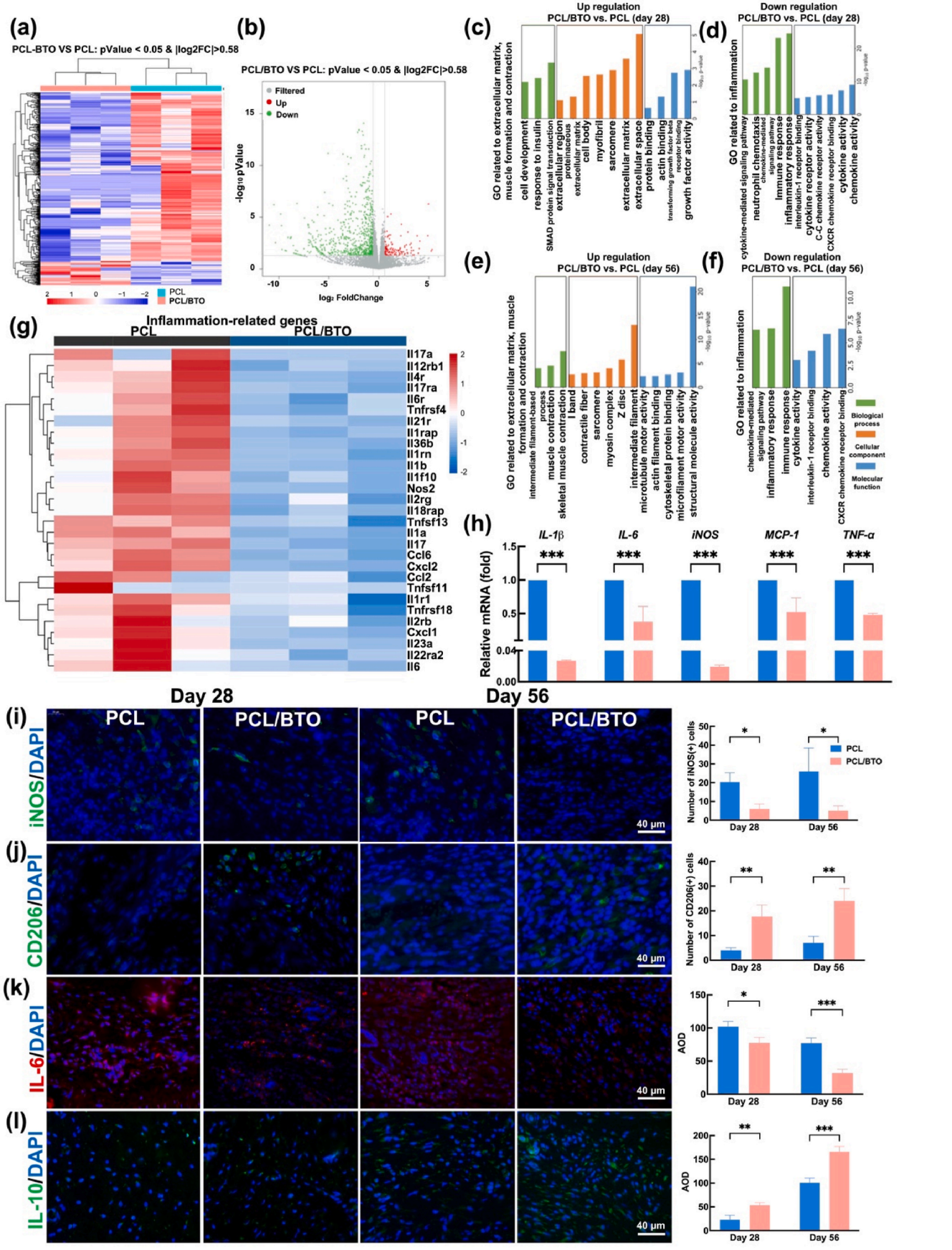

(caption on next page)

Fig. 7. PCL/BTO nanofilm inhibits inflammation *in vivo*. (a) Heatmap of differentially expressed genes (DEGs) in the repaired tendons of PCL and PCL/BTO groups at day 28 post-operation. Red areas represent upregulated DEGs, and blue areas represent downregulated DEGs. (b) Volcano plot of DEGs in the PCL and PCL/BTO groups at day 28 post-operation. Red represents upregulated DEGs, green represents downregulated DEGs, and gray represents filtered DEGs. The differential genes were assigned to three GO categories: biological process (green), cellular component (orange), and molecular function (blue). (c) & (e) GO terms related to tendon regeneration among the top 10 upregulated clusters of each category at days 28 and 56 post-operation, respectively. (d) & (f) GO terms related to inflammation among the top 10 upregulated clusters of each category at days 28 and 56 post-operation, respectively. (g) Heatmap of DEGs related to inflammation in the PCL and PCL/BTO groups at day 28 post-operation. Red areas represent upregulated DEGs, and blue areas represent downregulated DEGs. (h) RT-qPCR of several proinflammatory factors in the PCL and PCL/BTO groups at day 28 post-operation. (i–l) Immunofluorescent staining images of proinflammatory factors (iNOS and IL-6) and anti-inflammatory factors (CD206 and IL-10), along with their corresponding semiquantitative analysis results. Bar = 40 μm $*p < 0.05$, $**p < 0.01$ and $***p < 0.001$.

downstream NF-κB, which ultimately leads to the secretion of proinflammatory factors including IL-1β, and aggravates inflammation [55]. As shown, cholesterol-related DEGs, such as *apolipoprotein c4* (*Apoc4*), are significantly downregulated (Fig. 8b) in PCL/BTO group comparing to PCL group at day 28 post-operation. To assess cholesterol levels within the tendon tissue, we performed filipin staining. As shown in Fig. 8f and g, the cholesterol content is higher in the PCL group at the same time point, which is consistent with the detection of increased inflammation levels (Fig. 7).

During the repair of Achilles tendon defects, tendinopathy is one of the most common consequences of poor tendon repair and is characterized by heterotopic ossification, which impairs physical function [56]. Therefore, we also enriched genes related to osteogenesis and tenogenesis to evaluate the impact of piezoelectric stimulation on tenogenesis and osteogenesis. As shown in Fig. 8c and h, tendon formation–related genes such as *collagen type I alpha 1* chain (*COL1a1*), *fibromodulin (FMOD), tenomodulin (TNMD),* and *scleraxis (SCX)* are upregulated in the PCL/BTO group, while osteogenesis-related genes such as *Wnt family member 3* (*Wnt3*), *Wnt family member 4 (Wnt4), bone morphogenetic protein 8a* (*BMP8a*), and *SRY-box transcription factor 2* (*SOX2*) are downregulated at day 28 post-operation. Then, we also performed RT-qPCR detection of the expression of tendon development–associated genes, including *SCX*, *biglycan (BGN)*, *FMOD*, and *TNMD*, tendon maturation *including tenascin-C*, *decorin*, and *thrombospondin 4*, and collagen assembly associated genes including *lysyl oxidase (LOX), Col1a1, Col3a1, Col5a1*, and *Col6a1*. As shown in Fig. 8i, the expressions of these genes are significantly upregulated in the PCL/BTO group, indicating a better regeneration outcome at day 28 post-operation. Additionally, immunofluorescence analysis shown in Fig. S12 revealed increased TNMD expression, along with downregulation of the osteogenic marker OPN and the chondrogenic marker COL2. These findings suggest that the PCL/BTO membrane facilitates tendon regeneration and repair while prevents ossification, chondrification and tendinopathy.

In summary, piezoelectric PCL/BTO nanofilms promote tendon repair by inhibiting angiogenesis, reducing lipid deposition, further lowering inflammation, and decreasing the occurrence of ectopic ossification. Additionally, piezoelectric stimulation also facilitates tendon regeneration by upregulating tendon-related genes and enhancing collagen deposition and remodeling.

2.6. Piezoelectric stimulation reduces inflammation via IL-17A and NF-κB signaling

Tissue repair involves a large number of protein synthesis and energy metabolism processes. As shown, gene set enrichment analysis (GSEA) reveals that several pathways related to protein synthesis (ribosome pathway), energy metabolism (tricarboxylic acid cycle and pyruvate metabolism pathways), and collagen deposition (ECM-receptor interaction pathway) are upregulated (Fig. 8k–o) at day 28 post-operation. Ribosomal proteins are critical to cell growth, proliferation, and functional expression by regulating the synthesis of various proteins [57]. The upregulation of ribosomal proteins in the ribosome pathway could accelerate the protein synthesis to meet the requirements in the rapid repair stage of tissue regeneration. The tricarboxylic acid cycle is one of the most significant metabolic processes related to energy production, which converts carbohydrates and fats into adenosine triphosphates [58]. In addition to being a critical metabolite in cellular energy metabolism, pyruvate promotes tissue regeneration by reducing fibrosis and improving the expression of antioxidant enzymes [59]. Therefore, enhancing pyruvate metabolism can improve tendon healing and facilitate an earlier return to physical activity or sport. According to GSEA data (Fig. 8o), the lipoic acid metabolism pathway is also upregulated, leading to increased lipoic acid production, which helps scavenge and inactivate free radicals, thereby preventing collagen abnormalities in tendon tissues [60,61]. Therefore,the GSEA analysis results indicate that piezoelectric stimulation may positively influence protein synthesis and energy supply, both are conducive to tissue regeneration. Additionally, GSEA also displays several downregulated inflammation-related signaling pathways in the PCL/BTO group at day 28 post-operation, including cytokine–cytokine receptor interaction signaling pathway, TNF signaling pathway, NOD-like receptor signaling pathway, chemokine signaling pathway, IL-17 signaling pathway, and NF-κB signaling pathway (Fig. 8p–v).

Furthermore, when we explored the downregulated Kyoto Encyclopedia of Genes and Genomes (KEGG) pathway classification in the PCL/BTO groups versus PCL groups, DEGs related to the immune system account for the second highest percentage, only surpassed by those related to signal transduction (Fig. 8j). Screening of the key differential genes reveals the downregulation of *nfkb1* (*p50*), *nfkbia* (*IκBα*), and *Ikbkb* (*IKKβ*) in these downregulated inflammatory pathways (Fig. 8p–v), suggesting that piezoelectric stimulation inhibits the canonical NF-κB pathway. NF-κB is a family of inducible transcription factors that play a pivotal role in regulating the immune system by responding to various stimuli, including endogenous inflammatory signals like IL-1β and IL-17A and exogenous pathogen–derived substances like lipopolysaccharides [62].

Afterwards, we further explored the mechanism by which piezoelectric stimulation inhibits the inflammation at day 28 post-operation. The KEGG pathway analysis displays that the downregulated DEGs are mostly enriched in inflammation-regulated pathways, including IL-17 signaling pathway, TNF signaling pathway, NOD-like receptor signaling pathway, and NF-κB signaling pathway (Fig. 9a), which is consistent with the GSEA data. Moreover, the IL-17 signaling pathway exhibits the highest enrichment scores among all downregulated pathways. After IL-17A binds to its receptor (such as interleukin 17 receptor A), it activates downstream signaling pathways, including the NF-κB and mitogen-activated protein kinase pathways, and promotes the expression of proinflammatory cytokines and chemokines. These molecules can attract neutrophils to the site of inflammation and enhance the inflammatory response, resulting in excessive inflammation that can induce apoptosis of normal cells, further impairing tissue repair.

In this particular IL-17 mediated activation, the dimer (RelA and p50) can be activated through the canonical NF-κB pathway, inducing the production of proinflammatory cytokines such as IL-1β, TNF-α, and IL-6 [63]. The deteriorated inflammatory microenvironment caused by these factors may trigger many adverse consequences, including the inhibition of the repair process, increasing scarring, and accelerating tissue degeneration.

However, this study demonstrates that PCL/BTO nanofilms can

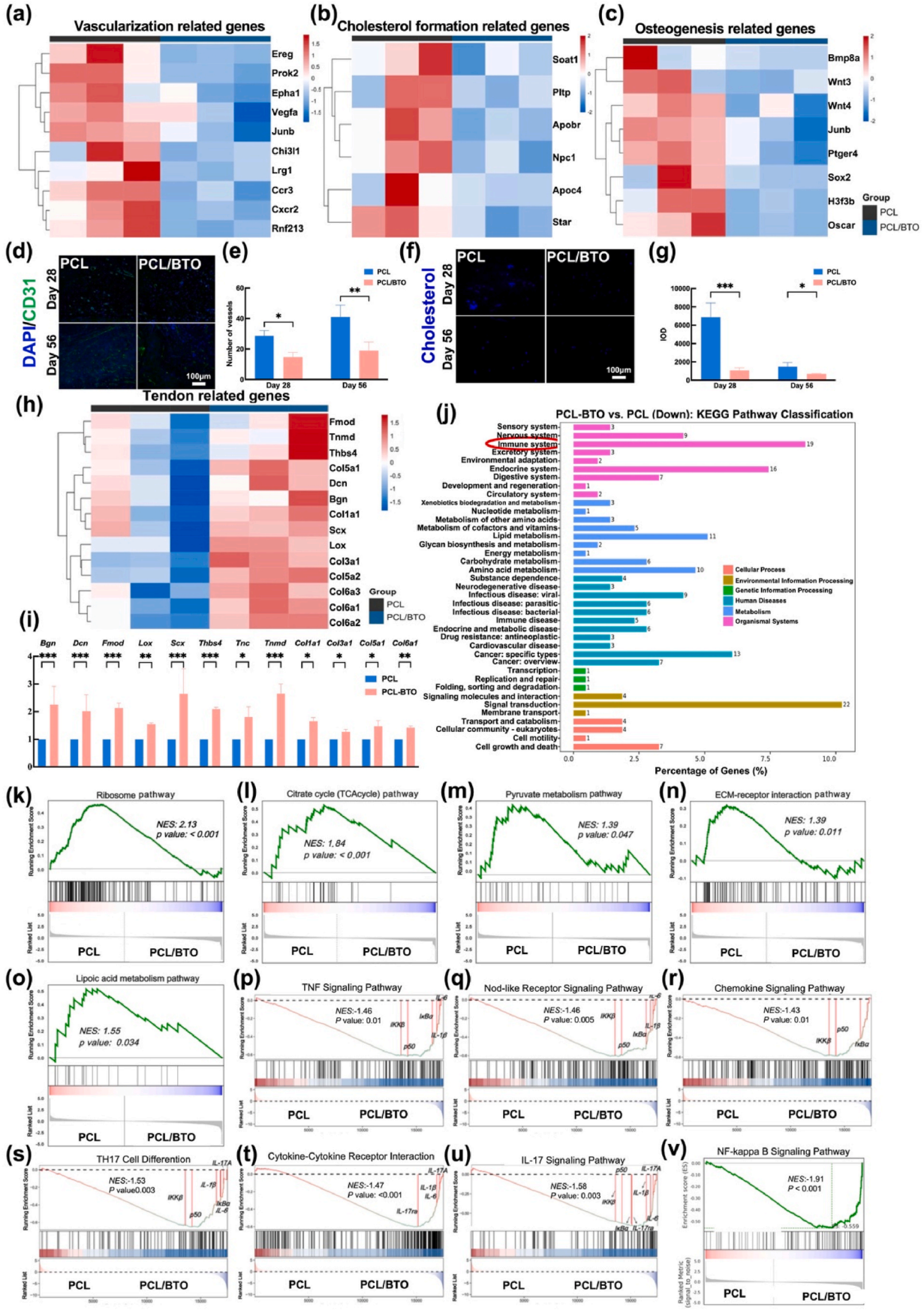

(caption on next page)

Fig. 8. PCL/BTO nanofilm inhibits excessive vascularization, cholesterol formation, ossification, and inflammation in regenerated tendon tissues at day 28 post-operation via multiple signaling pathways. (a) Heatmap of DEGs related to vascularization in the PCL and PCL/BTO groups at day 28 post-operation. (b) Heatmap of DEGs related to cholesterol formation in the PCL and PCL/BTO groups at day 28 post-operation. (c) Heatmap of DEGs related to osteogenesis in the PCL and PCL/BTO groups at day 28 post-operation. (d) Immunofluorescent staining of CD31 in the PCL and PCL/BTO groups and (e) semi-quantitative analysis. Bar = 100 μm. (f) Filipin staining in the PCL and PCL/BTO groups and (g) semi-quantitative analysis. Bar = 100 μm. (h) Heatmap of DEGs related to tenogenesis in the PCL and PCL/BTO groups at day 28 post-operation. (i) RT-qPCR detection of genes related to tenogenesis in the PCL and PCL/BTO groups at day 28 post-operation. (j) Downregulated KEGG pathway classification in the PCL and PCL/BTO groups at day 28 post-operation. Gene set enrichment analysis to show upregulated signaling pathway (k–o) and downregulated signaling pathway (p–v) in PCL/BTO groups at day 28 post-operation. $^{*}p < 0.05$, $^{**}p < 0.01$ and $^{***}p < 0.001$.

effectively downregulate several inflammation-related genes, including *IL-17A*, *p50*, *IκBα*, *IKKβ*, *IL-1β*, and *IL-6*. Immunofluorescence analysis further confirms that PCL/BTO nanofilms suppressed IL-17A and IL-17RA expression (Fig. S12), suggesting that piezoelectric stimulation may help reverse the inflammatory state and create an optimal microenvironment for tendon regeneration by inhibiting the IL-17A/NF-κB signaling pathway.

The cytokine IL-17A is secreted primarily by the immune cell subset of T helper 17 (Th17) cells, a specialized group of $CD3^+$ T cells that play a pivotal role in regulating immune responses, especially in inflammatory diseases [64,65]. As shown, the GSEA reveals that the Th17 cell differentiation signaling pathway is downregulated in the PCL/BTO group (Fig. 8s and u). The expression of genes that promote Th17 cell differentiation, such as IL-6 and IL-23a (Fig. 7g), are also reduced, which may inhibit IL-17A. Therefore, we performed flow cytometric analysis on neo-tendon tissues treated with PCL and PCL/BTO nanofilms at day 28 post-operation to assess IL-17A production and the proportion of $CD3^+$ T cells. Flow cytometry reveals that the proportion of $CD3^+$ T cells among total lymphocyte population in the neo-tendon of the PCL/BTO group (39.06 % ± 10.53 %) is decreased compared with that in the PCL group (78.24 % ± 6.51 %) (Fig. 9d and e, S13). Intracellular cytokine staining showed that IL-17 positive $CD3^+$ T cells are less in the PCL/BTO group than that in PCL group (5.24 % ± 2.91 % vs. 9.86 % ± 4.88 %) (Fig. 9f and g). These data suggest that the IL-17-producing T cells and IL-17A production are downregulated in the PCL/BTO group, which provides the evidence that IL-17A/NF-κB signaling pathway is inhibited by the piezoelectric effect.

Besides, a heatmap of DEGs related to the IL-17A/NF-κB signaling pathway is also generated. As shown in Fig. 9b, the expression of critical genes such as *IL-17A*, *TRAF6*, *IKKβ*, and *p50* are significantly reduced at day 28 post-operation. RT-qPCR analysis also confirms the significant downregulation of the genes of the IL-17 signaling pathway in the neo-tendon tissue at day 28 post-operation (Fig. 9c). To further support these findings, Western blot analysis was conducted to detect the phosphorylation of related proteins of the IL-17A/NF-κB signaling pathway in the neo-tendon tissue at day 28 post-operation, which shows that the relative phosphorylated IκBα (p-IκBα) protein content of the PCL group is three times higher than that of the PCL/BTO group, the relative p-IKKα protein content is two times higher in the PCL/BTO group, and the relative p-p50 protein content is also significantly higher than that of the PCL/BTO group (0.68 ± 0.09 vs. 0.46 ± 0.05) (Fig. 9h–k). These results demonstrate the inhibitory effect of piezoelectric stimulation on NF-κB-related protein activity at the protein level.

It has been demonstrated that a single circular RNA (circRNA)/long noncoding RNA (lncRNA) can affect several microRNAs (miRNAs) by acting as a miRNA sponge or competitive [66]. circRNA/lncRNA can induce multiple effects on the downstream mRNAs by amplifying the cascade reaction. Herein, we investigated the potential mechanism by which circRNA and lncRNA regulate the NF-κB-related mRNAs at day 28 post-operation. Fig. 9l shows that four downregulated differentially expressed lncRNAs (DElncRNAs) with associated miRNAs and the downstream mRNAs were used to build up a lncRNA–miRNA–mRNA interaction network. Among the top 10 upregulated BP, CC, and MF clusters, 13 are related to ECM and transcriptional regulation. These are related to protein synthesis and collagen deposition, affecting tendon regeneration and repair (Fig. S14a).

Among the downregulated top 10, seven clusters are related to inflammation, including the secretion of IL-6 and IL-8 and nitric oxide biosynthesis (Fig. S14b). IL-6 is an important initiating factor for Th17 cell differentiation, which is consistent with the results of GSEA analysis. To a certain extent, this also implies that piezoelectric stimulation affects lncRNA and triggers the changes in related mRNA and corresponding downstream signaling pathways, which provides new insights for subsequent related research. Moreover, five downregulated differentially expressed circRNAs (DEcircRNAs) with associated miRNAs and the downstream mRNAs were used to build up a circRNA–miRNA–mRNA interaction network (Fig. 9m). Five of the top 10 upregulated BP, CC, and MF clusters are related to cell proliferation or protein synthesis (Fig. S15a). Among the downregulated top 10, four clusters are related to inflammation and protein disassembly (Fig. S15b). These DEcircRNA and DElncRNA can be regarded as the candidates for further research in tendon injury inflammation. Overall, these findings demonstrate that the piezoelectric stimulation generated by PCL/BTO nanofilms can alleviate inflammation by inhibiting the activation of NF-κB, reducing the production of IL-17A, and thereby reducing the production of inflammatory factors in the tendon (Fig. 9n).

3. Conclusion

This study demonstrates that piezoelectric PCL/BTO nanofilms fabricated by coaxial electrospinning can reduce local inflammation and accelerate the repair of large tendon defects by inhibiting the expression of proinflammatory genes and enhancing the expression if tendon regeneration related genes. The nanofilms exhibit good mechanical properties and biocompatibility, the ability to reduce proinflammatory cytokines in macrophages under piezoelectric stimulation and the promoting effect on tendon regeneration and functional recovery with enhanced tissue quality and mechanical properties. Gene expression and transcriptome analysis demonstrates that the inhibition of NF-κB pathways as well as the inflammatory response by PCL/BTO mediated piezoelectric effect is mainly via blocking the IL-17A/NF-κB-pathway (Fig. 9n). Importantly, this study reveals the great potential of PCL/BTO nanofilms as a novel approach for tendon regeneration.

4. Experimental section

4.1. Preparation of three-dimensional (3D) piezoelectric coaxial electrospinning PCL/BTO nanofilms

Preparing coaxial PCL/BTO electrospinning film with core–shell structure required the preparation of core and shell solutions first as previously reported [67]. The shell solution was formed by 1g PCL dissolved in 10 mL of hexafluoroisopropyl alcohol. The core solution was formed by 0.05, 0.10, and 0.15 g BTO (3.33 %, 6.67 %, and 10 %) and 0.5 g of PCL dissolved in 10 mL of hexafluoroisopropyl alcohol, and the solution was stirred by a magnetic agitator for 12 h during the whole process. The polymeric solution was electrospun into nanofibers as the following parameters: applied voltage 15 kV, flow rate 0.5 mL/h, needle tip to drum-collector gap distance 16 cm, and ambient conditions (20°C-25 °C and 25%–30 % humidity). Then, the produced PCL and PCL/BTO nanofilms were subjected to vacuum-drying for later use.

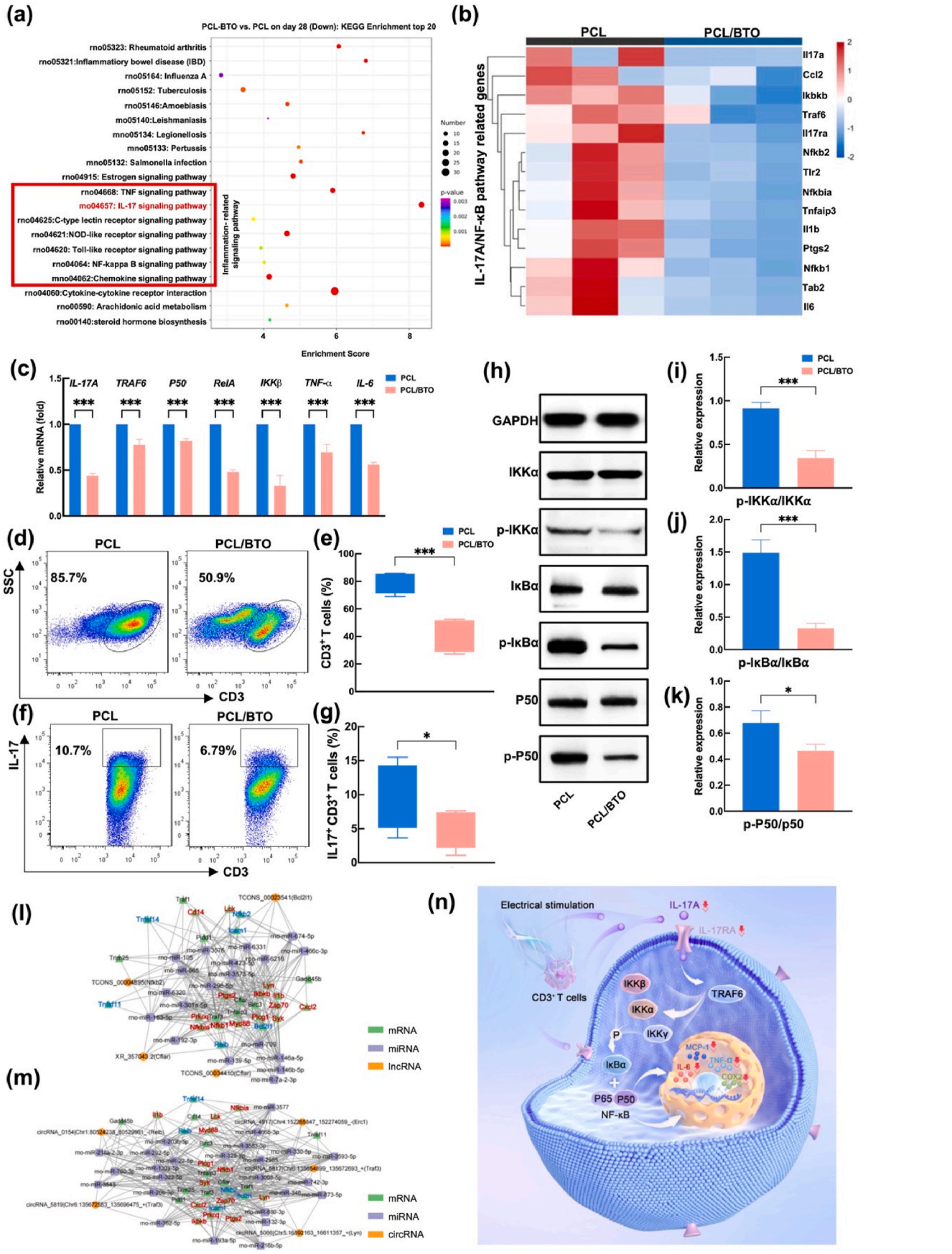

(caption on next page)

Fig. 9. PCL/BTO nanofilm suppresses inflammation via inhibiting the IL-17A/NF-κB signaling pathway (a) Downregulated KEGG enrichment of top 20 in the regenerated tendons of PCL/BTO groups vs. PCL groups at day 28 post-operation. (b) Heatmap of DEGs related to the IL-17A/NF-κB signaling pathway of the tendons at day 28 post-operation. (c) RT-qPCR detection of the genes in IL-17A/NF-κB signaling pathway of the tendons at day 28 post-operation. Flow cytometry detection of the proportion of (d) $CD3^+$ T cells, (f) IL-17^+ T cells of neo-tendons at day 28 post-operation. Quantitative analysis of flow cytometry of (e) $CD3^+$ T cells and (g) IL-17^+ T cells. (h) Western blotting of IKKα, IκBα, and p50 with GAPDH as an equal loading constant control and (i–k) their semi-quantitative analysis. (l) lncRNA–miRNA–mRNA interaction network. (m) circRNA–miRNA–mRNA interaction network. (n) Scheme of the mechanism of PCL/BTO nanofilm for inhibiting inflammation *in vivo*. Data are presented as mean ± SD. $*p < 0.05$ and $***p < 0.001$.

4.2. Characterization of 3D piezoelectric coaxial electrospinning PCL/BTO nanofilms

4.2.1. Surface morphology

The surface morphology of the PCL and PCL/BTO nanofibers was observed using SEM (Sigma 300, ZEISS). Before imaging, all samples were sputter-coated with gold for 30 s to increase substrate conductivity. To verify the distribution of BTO, the element mapping (C, O, Ba, and Ti) of PCL/BTO nanofibers was further employed by TEM (Quanta 200 FEI, Eindhoven, Netherlands) as previously reported [68].

As reported [69], to visually observe the morphology variation of samples, the surface topography and roughness of a single fiber were analyzed using an NT-MDT Prima Dimension FastScan AFM (Bruker, Germany). AFM images were generated by scanning with ScanAsyst mode using a silicon nitride probe. The roughness and average DMT modulus were measured from the obtained AFM images via NanoScope Analysis software.

4.2.2. Verification of piezoelectric performance of 3D films

To verify the piezoelectric performance, A PFM in contact mode was used to write a loop on the sample by applying different positive and negative voltages through a platinum-coated probe. The outer circle of the loop was written with a voltage of −40 V, and the inner circle was written with a +40 V DC voltage. The amplitude and phase changes of the written region were then read around the resonant frequency under the voltage of ±220 V. To measure the mechanical response of the composite membranes, all samples of 3D films (pure PCL nanofilms, polarized 3.33 %, 6.67 %, and 10 % PCL/BTO nanofilms) were cut into $3 \times 3\ cm^2$ sizes and attached to copper membranes of different sizes. The copper membranes were then attached to the front and back of the composite film, respectively, corresponding to the positive and negative electrodes. During the measurement process, the composite membrane was fixed on a pulling device and subjected to mechanical stimulation to simulate tendon movement with 4 % stretching at a frequency of 2 Hz. A mechanical stimulation device was designed to apply longitudinal force to the composite diaphragm in an animal model. The diaphragm was knocked at different frequencies and forces, and the resulting current output was recorded by a computer.

4.2.3. CCK-8 cell proliferation assay and macrophage culturing

RAW 264.7 macrophages were cultured in Dulbecco's Modified Eagle Medium (DMEM, Gibco) supplemented with 10 % fetal bovine serum (FBS, Gibco) and 1 % penicillin-streptomycin (Invitrogen) as reported [70]. Cells were maintained in a humidified incubator at 37 °C with 5 % CO_2. For experiments, macrophages were seeded at a density of 1×10^5 cells/cm^2 in culture plates or on the surface of PCL and PCL/BTO nanofilms. The medium was replaced every 2 days, and cells were allowed to adhere overnight before further treatment.

To analyze the effects of electrical stimulation on cell proliferation, macrophages and tenocytes were seeded on PCL and PCL/BTO nanofilms for 3 days with or without electrical stimulation. The nanofilms were first soaked in 75 % ethanol for 30 min and then sterilized under ultraviolet light for 45 min. PCL nanofilms and PCL/BTO nanofilms were cut to the size of 1.5 × 4.5 cm and fixed to the bioreactor. RAW 264.7 macrophages were seeded onto 3D nanofilms with the density of 5×10^4 cells per chamber. And tenocytes were seeded onto 3D nanofilms with the density of 1×10^4 cells per chamber. Macrophages and tenocytes were starved in serum-free medium for 12 h to allow for cell synchronization, then they were replaced with fresh DMEM medium containing 10 % FBS and 1 % penicillin/streptomycin. Except for static culture (PCL-S and PCL/BTO-S), two different nanofilms (PCL-ST and PCL/BTO-ST) were installed on the bioreactor and subjected to periodic deformation by external forces of a certain frequency (2 Hz and 4 % strain magnitude) to get stretched. Then the proliferation was tested with a CCK-8 (Dojindo, Kumamoto, Japan) at days 1 and 3. Briefly, at each testing time point, 200 μl of sterile CCK-8 solution mixed with 2000 μL medium was added to each bioreactor chamber and incubated for 2 h at 37 °C. Then 100 μL of the mixture was transferred to 96-well plate for detection. The optical density values of the medium were evaluated at a wavelength of 450 nm using a microplate reader (Thermo Scientific). All assays were performed in quintuplicate and repeated in three cell samples [46].

4.2.4. SEM analysis of cell morphology on nanofibers

Macrophages were seeded on 3D nanofilms at the density of 5×10^4 cells per chamber. The cell culture method was the same as described in *4.2.3*. Then, they were fixed after 24 h of culture. The cell-seeded nanofilms were first fixed in 2.5 % glutaraldehyde overnight (4 °C) and were then rinsed three times with PBS. Then, those fibers were sequentially dehydrated in 25 %, 50 %, 75 %, 95 % and 100 % alcohol for 20 min. After that, nanofibers were put into the oven at 60 °C for 5 min to get dried. Those fibers were sputter-coated with gold, and their morphology was examined with SEM (PhilipsXL-30, The Netherlands) [68].

4.2.5. Cytoskeleton staining

After culturing on two 3D nanofilms and being stretched for 3 days, the seeded macrophages were fixed in 4 % paraformaldehyde (Biosharp, China) for 30 min, and then permeated with 0.1 % Triton X-100 (Solarbio, China) for 10 min. After being washed thoroughly with PBS, the cytoskeleton was stained using TRITC Phalloidin (1:200 dilution, Yeasen Biotechnology, China) for 30 min, and the cell nuclei were stained with DAPI (1:1000 dilution, Yeasen Biotechnology, China) for 10 min at room temperature. Afterwards, the cytoskeleton was observed using laser-scanning confocal microscopy.

4.3. RNA extraction and transcriptome analysis

The tendon samples were collected at days 28 and 56 post-operation, and the total RNA was extracted using the TRIzol reagent. The purity and quantification of RNA were identified by spectrophotometer, and the integrity of RNA was evaluated by Agilent 2100 Bioanalyzer. Using VAHTS Universal V5 RNA-seq Library Prep kit to construct transcriptional library according to the instructions. Principal component analysis was performed using R software (v3.2.0) to evaluate the biological duplication of samples. Differential expression analysis was performed using the DESeq25. A p value < 0.05 was set as the threshold for significant DEGs. Hierarchical cluster analysis of DEGs was performed using R software (v3.2.0) to demonstrate the expression pattern of genes in different groups and samples, including GO functional annotation and enrichment analysis. KEGG pathway analysis was performed to enrich the higher functional molecules defined in biological systems.

4.4. RT-qPCR

RAW 264.7 macrophages were treated in the same way as described

in *4.2.3*. The tendon tissues were harvested on 28 day post-operation. For cells and tendon tissues, after RNA extraction, the complementary deoxyribonucleic acid was synthesized from 1000 ng total RNA of each sample with AMV reverse transcriptase (Takara, Japan) in 20-μL reaction solution, which was composed of 4 μL of 5 × buffer, 2 μL of deoxynucleoside triphosphate, 1 μL of oligo-(dT), 0.5 μL of RNase inhibitor, and 0.5 μL of AMV reverse transcriptase, and then double-distilled water was added to meet the final volume. Then, the mixture was incubated at 30 °C for 10 min, 42 °C for 60 min, 95 °C for 5 min, and 5 °C for 5 min. Complementary deoxyribonucleic acid was amplified to determine the gene expression levels using a Power SYBR Green PCR master mix (2 ×) (Applied Biosystems, Foster City, CA) in a real-time thermal cycler (QuantStudio 6-flex, Thermo Fischer Scientific). It was performed with 95 °C for 5 min, then 40 cycles at 95 °C for 10 s, followed by 60 °C for 30 s. The optimized primers for RT-qPCR analyses are listed in Supplementary Table 1. Each gene of interest was normalized to glyceraldehyde-3-phosphate dehydrogenase, and the fold change was compared to that of the control sample. Each assay was performed in triplicate, and experiments were repeated in at least three pooled cell samples.

4.5. Animal experiments

The animal experiment**al** protocol was approved by the Ethics Committee of Shanghai Ninth People's Hospital (approval number: SH9H-2022-A391-SB). Thirty-three Sprague Dawley rats (Shanghai Jiagan Biological Technology Co., Ltd) were divided into two groups. The operations for animal handling were approved by the Animal Care and Experiment Committee of Shanghai Ninth People's Hospital. Surgical sutures were performed as described previously [68]. After the rats were anesthetized with phenobarbital sodium (30 mg/kg), a 6 mm segment of the Achilles tendon was excised to create a critical-sized defect. Scaffold sheets were shaped into rods measuring 0.6 cm in length and 0.2 cm in diameter and were designed to fit the defect site precisely. Afterwards, the scaffolds were anchored in place using 5–0 non-resorbable sutures to bridge the gap. To ensure proper alignment and secure fixation, a Kessler core suture technique was applied to connect the scaffold to the severed tendon ends. This approach provided robust mechanical stability and promoted scaffold integration with the native tendon tissue. After suturing, the wound was closed to maintain the construct's position and support the healing process. The rats were sacrificed under anesthesia at days 28 and 56 post-surgery for harvesting the repaired tendons.

4.6. Histologic analysis and immunohistochemical staining

At days 28 and 56 post-operation, tendon samples of the two groups were collected, fixed with 4 % paraformaldehyde at 4 °C overnight, embedded in paraffin, and continuously sliced with a 5 μm thickness. HE staining (Beyotime Biotechnology, China), Masson's trichrome staining (Nanjing Jiancheng Bioengineering Institute, China), and Sirius red staining (Solarbio, China) were performed to test the amount, type, and structure of collagens according to the instructions. The expression of platelet endothelial cell adhesion molecule-1 (CD31), TNF-α, COL-1, and IL-6 were evaluated using immunofluorescence staining to verify the angiogenesis, inflammation, and collagen deposition. Additionally, cholesterol staining was performed using immuno-fluorescence. The stained tissue sections were photographed using fluorescence microscopy, the average optical density value (AOD) and the integrated optical density (IOD) of each tissue slice were calculated from three randomly selected fields of view. In addition, the four-point scoring system, composed of scores 0 (normal), 1 (slightly abnormal), 2 (moderately abnormal), and 3 (considerably abnormal), was applied to evaluate the regenerated fiber structure and fiber arrangement.

To observe the superstructure of the regenerated tendons, tendons harvested at days 28 and 56 postsurgery were subjected to TEM (Quanta 200 FEI, Eindhoven, Netherlands) examination ($n = 3$ for each group) in the cross-section. The quantified average fibril diameter was calculated using the ImageJ analysis software from the obtained images [68]. Additionally, the mechanical properties of the fresh tendons were analyzed with a biomechanical analyzer (Instron 4411, Canton, MA) to calculate the data of Max load (N), Tensile strength (MPa), and Young's modulus (MPa). For each group, at least three samples were tested [68].

4.7. Flow cytometry analysis

The regenerated tendon tissues were minced and treated with digestion buffer containing collagenase IV, hyaluronidase, and DNase I at 37 °C for 30 min, and then the single-cell suspensions were washed and collected for further experiments. Single-cell suspensions were stained with fluorescence-labeled antibodies, including viability dye (Invitrogen, 65-0865-14), CD3 (Biolegend, 201403), CD4 (Biolegend, 201509), and CD8a (Biolegend, 201712). To detect intracellular cytokine IL-17, the cells were surface-stained with the above antibodies, fixed, and then intracellularly stained with IL-17A (Invitrogen, 25-7177-82). Cells were harvested and analyzed using a FACSCanto II flow cytometer [71].

4.8. Western blotting

The neo-tendons harvested at day 28 post-operation were collected and lysed in radioimmunoprecipitation assay lysis buffer for total protein extraction. Subsequently, the harvested proteins were quantified using the bicinchoninic acid protein assay kit, separated using 10 % (sodium dodecyl sulfate–polyacrylamide gel electrophoresis, and transferred onto a Polyvinylidene fluoride (PVDF) membrane. Then, the PVDF membrane was blocked with 5 % bovine serum albumin and incubated with an inhibitor of NF-κB kinase subunit alpha (IKKα) antibody (1:600, Affinity, AF6014), a phosphorylated inhibitor of NF-κB kinase subunit alpha (p-IKKα) antibody (1:800, Affinity, AF3014), inhibitory kappa-B alpha (IκBα) antibody (1:800, Huabio, ET1603-6), phosphorylated inhibitory kappa-B alpha (p-IκBα) antibody (1:700, Huabio, HA721802), NF kappa-B p105/p50 (nfkb1, p50) antibody (1:800, Affinity, AF6217), Phospho-NF kappa-B p105/p50 (p-nfkb1, p-p50) antibody (1:800, Affinity, AF 3219), and antihuman GAPDH antibody (1:5000, Affinity, AF7021) overnight at 4 °C. After that, the PVDF membrane was washed with PBST and incubated with the goat anti-rabbit IgG/horseradish peroxidase antibody (1:2000, Affinity, T0004) for 1 h at room temperature. Finally, the protein bands were visualized using an enhanced chemiluminescence detection system [72].

4.9. Subcutaneous implantation experiment

To determine the biocompatibility and biological performance of the two nanofilms *in vivo,* subcutaneous implantation was conducted in the abdominal site of Sprague Dawley rats. Before implantation, all nanofilms were cut into 1 × 1 cm pieces, then sterilized with 70 % ethanol for 30 min, followed by ultraviolet radiation for 30 min. Two pieces of PCL nanofilms and two pieces of PCL/BTO nanofilms were implanted subcutaneously in the abdomen of each rat. After 14 and 28 days of implantation, nanofilms were explanted for histological evaluation. Samples were cut into cross-sections and stained with HE. Immunofluorescent staining of iNOS, IL-6, IL-10, and CD206 was also performed to assess the inflammation at the nanofilm-tissue interface.

4.10. Gait experiment

On the 14th, 28th, and 56th day post-operation, a gait experiment was used to test the motor function recovery. The rats were placed on a treadmill with a rotation speed of 10 cm/s, and the rats' continuous gait was recorded for at least 15 s. Repetitive gait experiments were performed using a computerized gait analysis system (Digigait Imaging

System, Mouse Specifics, Inc., USA). DigiGait imaged the ventral view of rats walking on a motorized transparent treadmill belt and automatically calculated different gait metrics to evaluate the recovery of the rat's Achilles tendon. The AFI was used to assess the gait pattern after an Achilles tendon segmental resection and subsequent repair. An AFI value closer to zero is the indicative of better recovery. Print length, the distance between the first and fifth toes or toe spreading, and the distance between the second and fourth toes or intermediary toes (IT) were measured. Print length factor (PLF), toe spread factor (TSF), intermediate toe spread factor (ITF), and AFI were calculated according to the following formulas described previously [73].

$$PLF = \frac{PLN - PLP/B}{PLP/B}$$

$$TSF = \frac{TSN - TSP/B}{TSP/B}$$

$$ITF = \frac{ITSN - ITSP/B}{ITSP/B}$$

$$\mathrm{AFI} = 74(\mathrm{PLF}) + 48(\mathrm{ITF}) + 161(\mathrm{TSF}) - 5$$

4.11. Statistical analysis

All quantitative data are expressed as mean ± standard deviation. Data are statistically evaluated using Student's t-test (two groups) and one-way ANOVA followed by Bonferroni's test (multiple groups) using SPSS software (version 19.0, SPSS Inc., IL, USA). It is considered statistically significant when the obtained p value is less than 0.05 and is indicated as: $^{*}p < 0.05$, $^{**}p < 0.01$, and $^{***}p < 0.001$. All experiments were repeated at least three times.

CRediT authorship contribution statement

Wufei Dai: Writing – original draft, Visualization, Methodology, Investigation, Formal analysis, Data curation, Conceptualization. **Qi Xu:** Software, Methodology, Formal analysis. **Qinglin Li:** Data curation, Formal analysis, Software. **Xiansong Wang:** Validation, Investigation, Supervision. **Wenjie Zhang:** Supervision, Investigation, Validation. **Guangdong Zhou:** Supervision, Investigation, Validation. **Xu Chen:** Funding acquisition, Data curation, Formal analysis, Supervision, Writing – original draft. **Wei Liu:** Writing – review & editing, Supervision, Project administration, Funding acquisition, Conceptualization, Methodology. **Wenbo Wang:** Writing – review & editing, Supervision, Project administration, Funding acquisition, Conceptualization, Data curation, Formal analysis, Investigation, Methodology, Validation.

Data Availability statement

The data that support the findings of this study are available from the corresponding author upon reasonable request.

Ethics approval and consent to participate

The animal experiment protocol was approved by the Ethics Committee of Shanghai Ninth People's Hospital (approval number: SH9H-2022-A391-SB).

Funding sources

This study was supported by the National Natural Science Foundation of China (31870967 to Wei Liu and 81701841 to Wenbo Wang) and the National Key R&D Program of China (2018YFC1105800 to Wei Liu). Xu Chen was supported by the Shanghai Pujiang Program (23PJD047) and the on-job postdoctoral program.

Declaration of competing interest

The authors declare no conflict of interest.

Acknowledgments

The authors would also thank Prof. Hairong Liu (Hunan University) for his kind help in providing the reactor.

Appendix A. Supplementary data

Supplementary data to this article can be found online at https://doi.org/10.1016/j.bioactmat.2025.02.038.

References

[1] M. O'Brien, The anatomy of the Achilles tendon, Foot Ankle Clin. 10 (2) (2005) 225–238, https://doi.org/10.1016/j.fcl.2005.01.011.
[2] B. Meulenkamp, D. Stacey, D. Fergusson, B. Hutton, R.S. Mlis, I.D. Graham, Protocol for treatment of Achilles tendon ruptures; a systematic review with network meta-analysis, Syst. Rev. 7 (1) (2018) 247, https://doi.org/10.1186/s13643-018-0912-5.
[3] J. Hou, R. Yang, I. Vuong, F. Li, J. Kong, H.Q. Mao, Biomaterials strategies to balance inflammation and tenogenesis for tendon repair, Acta Biomater. 130 (2021) 1–16, https://doi.org/10.1016/j.actbio.2021.05.043.
[4] Y. Huang, B. He, L. Wang, B. Yuan, H. Shu, F. Zhang, L. Sun, Bone marrow mesenchymal stem cell-derived exosomes promote rotator cuff tendon-bone healing by promoting angiogenesis and regulating M1 macrophages in rats, Stem Cell Res. Ther. 11 (1) (2020) 496, https://doi.org/10.1186/s13287-020-02005-x.
[5] J.H. Rho, I.G. Ko, J.J. Jin, L. Hwang, S.H. Kim, J.Y. Chung, T.J. Hwang, J.H. Han, Polydeoxyribonucleotide ameliorates inflammation and apoptosis in achilles tendon-injury rats, Int Neurourol J 24 (Suppl 2) (2020) 79–87, https://doi.org/10.5213/inj.2040428.214.
[6] N.L. Millar, K.G. Silbernagel, K. Thorborg, P.D. Kirwan, L.M. Galatz, G.D. Abrams, G.A.C. Murrell, I.B. McInnes, S.A. Rodeo, Tendinopathy, Nat. Rev. Dis. Primers 7 (1) (2021) 1, https://doi.org/10.1038/s41572-020-00234-1.
[7] S.J. Cui, Y. Fu, Y. Liu, X.X. Kou, J.N. Zhang, Y.H. Gan, Y.H. Zhou, X.D. Wang, Chronic inflammation deteriorates structure and function of collagen fibril in rat temporomandibular joint disc, Int. J. Oral Sci. 11 (1) (2019) 2, https://doi.org/10.1038/s41368-018-0036-8.
[8] I.C. Lawrance, L. Maxwell, W. Doe, Inflammation location, but not type, determines the increase in TGF-beta1 and IGF-1 expression and collagen deposition in IBD intestine, Inflamm. Bowel Dis. 7 (1) (2001) 16–26, https://doi.org/10.1097/00054725-200102000-00003.
[9] M.D. Shoulders, R.T. Raines, Collagen structure and stability, Annu. Rev. Biochem. 78 (2009) 929–958, https://doi.org/10.1146/annurev.biochem.77.032207.120833.
[10] S.M. Krane, Collagenases and collagen degradation, J. Invest. Dermatol. 79 (Suppl 1) (1982) 83s–86s, https://doi.org/10.1111/1523-1747.ep12545849.
[11] S. Chen, S. Jiang, W. Zheng, B. Tu, S. Liu, H. Ruan, C. Fan, RelA/p65 inhibition prevents tendon adhesion by modulating inflammation, cell proliferation, and apoptosis, Cell Death Dis. 8 (3) (2017) e2710, https://doi.org/10.1038/cddis.2017.135.
[12] Z.X. Yao, Y. Qian, Y. Jin, S.K. Wang, J.H. Li, W.E. Yuan, C.Y. Fan, Biomimetic multilayer polycaprolactone/sodium alginate hydrogel scaffolds loaded with melatonin facilitate tendon regeneration, Carbohydr. Polym. 277 (2022) 118865, https://doi.org/10.1016/j.carbpol.2021.118865.
[13] M.E. Ogle, C.E. Segar, S. Sridhar, E.A. Botchwey, Monocytes and macrophages in tissue repair: implications for immunoregenerative biomaterial design, Exp. Biol. Med. 241 (10) (2016) 1084–1097, https://doi.org/10.1177/1535370216650293.
[14] E. Mariani, G. Lisignoli, R.M. Borzì, L. Pulsatelli, Biomaterials: foreign bodies or tuners for the immune response? Int. J. Mol. Sci. 20 (3) (2019) 636, https://doi.org/10.3390/ijms20030636.
[15] A. Mauro, V. Russo, L. Di Marcantonio, P. Berardinelli, A. Martelli, A. Muttini, M. Mattioli, B. Barboni, M1 and M2 macrophage recruitment during tendon regeneration induced by amniotic epithelial cell allotransplantation in ovine, Res. Vet. Sci. 105 (2016) 92–102, https://doi.org/10.1016/j.rvsc.2016.01.014.
[16] R.J. Miron, D.D. Bosshardt, OsteoMacs: key players around bone biomaterials, Biomaterials 82 (2016) 1–19, https://doi.org/10.1016/j.biomaterials.2015.12.017.
[17] M.R. Cho, H.S. Thatte, R.C. Lee, D.E. Golan, Integrin-dependent human macrophage migration induced by oscillatory electrical stimulation, Ann. Biomed. Eng. 28 (3) (2000) 234–243, https://doi.org/10.1114/1.263.
[18] Z. Wang, L. Yu, B. Huang, S. Wang, K. Liao, G. Saren, X. Zhou, H. Jiang, Low-level transcutaneous electrical stimulation of the auricular branch of vagus nerve ameliorates left ventricular remodeling and dysfunction by downregulation of matrix metalloproteinase 9 and transforming growth factor β1, J. Cardiovasc. Pharmacol. 65 (4) (2015) 342–348, https://doi.org/10.1097/fjc.0000000000000201.

[19] K. Kapat, Q.T.H. Shubhra, M. Zhou, S. Leeuwenburgh, Piezoelectric nano-biomaterials for biomedicine and tissue regeneration, Adv. Funct. Mater. 30 (44) (2020) 1909045, https://doi.org/10.1002/adfm.201909045.

[20] A. Poudel, M.A. Fernandez, S.A.M. Tofail, M.J.P. Biggs, Boron nitride nanotube addition enhances the crystallinity and cytocompatibility of PVDF-TrFE, Front. Chem. 7 (2019) 364, https://doi.org/10.3389/fchem.2019.00364.

[21] G.B. Xia, G.B. Wang, H.Y. Yang, W.B. Wang, J. Fang, Piezoelectric charge induced hydrophilic poly(L-lactic acid) nanofiber for electro-topographical stimulation enabling stem cell differentiation and expansion, Nano Energy 102 (2022), https://doi.org/10.1016/j.nanoen.2022.107690, 10.1016/j.nanoen.2022.107690.

[22] R. Das, T.T. Le, B. Schiff, M.T. Chorsi, J. Park, P. Lam, A. Kemerley, A.M. Supran, A. Eshed, N. Luu, N.G. Menon, T.A. Schmidt, H. Wang, Q. Wu, M. Thirunavukkarasu, N. Maulik, T.D. Nguyen, Biodegradable piezoelectric skin-wound scaffold, Biomaterials 301 (2023) 122270, https://doi.org/10.1016/j.biomaterials.2023.122270.

[23] P. Wu, C. Xu, X. Zou, K. Yang, Y. Xu, X. Li, X. Li, Z. Wang, Z. Luo, Capacitive-coupling-responsive hydrogel scaffolds offering wireless in situ electrical stimulation promotes nerve regeneration, Adv. Mater. 36 (14) (2024) e2310483, https://doi.org/10.1002/adma.202310483.

[24] F.Y. McWhorter, T. Wang, P. Nguyen, T. Chung, W.F. Liu, Modulation of macrophage phenotype by cell shape, Proc. Natl. Acad. Sci. U.S.A. 110 (43) (2013) 17253–17258, https://doi.org/10.1073/pnas.1308887110.

[25] U. Arif, S. Haider, A. Haider, N. Khan, A.A. Alghyamah, N. Jamila, M.I. Khan, W. A. Almasry, I.K. Kang, Biocompatible polymers and their potential biomedical applications: a review, Curr. Pharm. Des. 25 (34) (2019) 3608–3619, https://doi.org/10.2174/1381612825999191011105148.

[26] S.W. Ibrahim, T.I. Hamad, J. Haider, Biological properties of polycaprolactone and barium titanate composite in biomedical applications, Sci. Prog. 106 (4) (2023) 368504231215942, https://doi.org/10.1177/00368504231215942.

[27] Y. Li, X. Dai, Y. Bai, Y. Liu, Y. Wang, O. Liu, F. Yan, Z. Tang, X. Zhang, X. Deng, Electroactive BaTiO(3) nanoparticle-functionalized fibrous scaffolds enhance osteogenic differentiation of mesenchymal stem cells, Int. J. Nanomed. 12 (2017) 4007–4018, https://doi.org/10.2147/ijn.S135605.

[28] E. Mancuso, L. Shah, S. Jindal, C. Serenelli, Z.M. Tsikriteas, H. Khanbareh, A. Tirella, Additively manufactured BaTiO(3) composite scaffolds: a novel strategy for load bearing bone tissue engineering applications, Mater. Sci. Eng., C 126 (2021) 112192, https://doi.org/10.1016/j.msec.2021.112192.

[29] P. Xu, B. Deng, B. Zhang, Q. Luo, G. Song, Stretch-induced tenomodulin expression promotes tenocyte migration via F-actin and chromatin remodeling, Int. J. Mol. Sci. 22 (9) (2021), https://doi.org/10.3390/ijms22094928.

[30] D.Q. He, F.L. Liu, S.J. Cui, N. Jiang, H.J. Yu, Y.H. Zhou, Y. Liu, X.X. Kou, Mechanical load-induced H_2S production by periodontal ligament stem cells activates M1 macrophages to promote bone remodeling and tooth movement via STAT1, Stem Cell Res. Ther. 11 (1) (2020), https://doi.org/10.1186/s13287-020-01607-9.

[31] B.T. van Dijk, A.M.P. Boeren, S.J.H. Khidir, N.K. den Hollander, A.H.M. van der Helm-van Mil, Work-related physical strain and development of joint inflammation in the trajectory of emerging inflammatory and rheumatoid arthritis: a prospective cohort study, RMD Open 10 (2) (2024) e003895, https://doi.org/10.1136/rmdopen-2023-003895.

[32] T. Panciera, L. Azzolin, M. Cordenonsi, S. Piccolo, Mechanobiology of YAP and TAZ in physiology and disease, Nat. Rev. Mol. Cell Biol. 18 (12) (2017) 758–770, https://doi.org/10.1038/nrm.2017.87.

[33] H. Liu, J. Hu, Q. Zheng, X. Feng, F. Zhan, X. Wang, G. Xu, F. Hua, Piezo1 channels as force sensors in mechanical force-related chronic inflammation, Front. Immunol. 13 (2022) 816149, https://doi.org/10.3389/fimmu.2022.816149.

[34] S. Chen, S.C. Jiang, W. Zheng, B. Tu, S. Liu, H.J. Ruan, C.Y. Fan, RelA/p65 inhibition prevents tendon adhesion by modulating inflammation, cell proliferation, and apoptosis, Cell Death Dis. 8 (3) (2017) e2710, https://doi.org/10.1038/cddis.2017.135.

[35] N. Tachibana, R. Chijimatsu, H. Okada, T. Oichi, Y. Taniguchi, Y. Maenohara, J. Miyahara, H. Ishikura, Y. Iwanaga, Y. Arino, K. Nagata, H. Nakamoto, S. Kato, T. Doi, Y. Matsubayashi, Y. Oshima, A. Terashima, Y. Omata, F. Yano, S. Maeda, S. Ikegawa, M. Seki, Y. Suzuki, S. Tanaka, T. Saito, RSPO2 defines a distinct undifferentiated progenitor in the tendon/ligament and suppresses ectopic ossification, Sci. Adv. 8 (33) (2022), https://doi.org/10.1126/sciadv.abn2138.

[36] D. Jeong, J. Lee, Y.-S. Yi, Y. Yang, K.W. Kim, J.Y. Cho, p38/AP-1 pathway in lipopolysaccharide-induced inflammatory responses is negatively modulated by electrical stimulation, Mediat. Inflamm. 2013 (2013) 1–11, https://doi.org/10.1155/2013/183042.

[37] Y. Kong, F. Liu, B. Ma, J. Duan, W. Yuan, Y. Sang, L. Han, S. Wang, H. Liu, Wireless localized electrical stimulation generated by an ultrasound-driven piezoelectric discharge regulates proinflammatory macrophage polarization, Adv. Sci. 8 (13) (2021) 2100962, https://doi.org/10.1002/advs.202100962.

[38] X. Liu, X. Wan, B. Sui, Q. Hu, Z. Liu, T. Ding, J. Zhao, Y. Chen, Z.L. Wang, L. Li, Piezoelectric hydrogel for treatment of periodontitis through bioenergetic activation, Bioact. Mater. 35 (2024) 346–361, https://doi.org/10.1016/j.bioactmat.2024.02.011.

[39] A.H. Lin, C.A. Slater, C.J. Martinez, S.J. Eppell, S.M. Yu, J.A. Weiss, Collagen fibrils from both positional and energy-storing tendons exhibit increased amounts of denatured collagen when stretched beyond the yield point, Acta Biomater. 155 (2023) 461–470, https://doi.org/10.1016/j.actbio.2022.11.018.

[40] K.H.L. Kwan, K.W.K. Yeung, X.L. Liu, K.K.Y. Wong, H.C. Shum, Y.W. Lam, S. H. Cheng, K.M.C. Cheung, M.K.T. To, Silver nanoparticles alter proteoglycan expression in the promotion of tendon repair, Nanomedicine 10 (7) (2014) 1375–1383, https://doi.org/10.1016/j.nano.2013.11.015.

[41] Y. Sun, R. Sheng, Z. Cao, C. Liu, J. Li, P. Zhang, Y. Du, Q. Mo, Q. Yao, J. Chen, W. Zhang, Bioactive fiber-reinforced hydrogel to tailor cell microenvironment for structural and functional regeneration of myotendinous junction, Sci. Adv. 10 (17) (2024) eadm7164, https://doi.org/10.1126/sciadv.adm7164.

[42] M.Z. Zhang, H.C. Liu, Q.B. Cui, P.L. Han, S.L. Yang, M.Y. Shi, T.T. Zhang, Z. A. Zhang, Z.Z. Li, Tendon stem cell-derived exosomes regulate inflammation and promote the high-quality healing of injured tendon, Stem Cell Res. Ther. 11 (1) (2020), https://doi.org/10.1186/s13287-020-01918-x.

[43] J. Sapudom, S. Karaman, B.C. Quartey, W.K.E. Mohamed, N. Mahtani, A. Garcia-Sabaté, J. Teo, Collagen fibril orientation instructs fibroblast differentiation via cell contractility, Adv. Sci. 10 (22) (2023) e2301353, https://doi.org/10.1002/advs.202301353.

[44] F. Giacomini, D.B. Barata, H.S. Rho, Z.T. Birgani, C. van Blitterswijk, S. Giselbrecht, R. Truckenmüller, P. Habibovic, Microfluidically aligned collagen to maintain the phenotype of tenocytes in vitro, Adv. Healthcare Mater. 13 (6) (2024) e2303672, https://doi.org/10.1002/adhm.202303672.

[45] D. Wallach, T.B. Kang, A. Kovalenko, Concepts of tissue injury and cell death in inflammation: a historical perspective, Nat. Rev. Immunol. 14 (1) (2014) 51–59, https://doi.org/10.1038/nri3561.

[46] W.F. Dai, B.Y. Zhou, B.C. Yi, W.J. Zhang, G.D. Zhou, Y.J. Hua, W.B. Wang, W. Liu, A novel TCR hydrogel wound dressing loaded with UC-SMC extract enhances skin regeneration and prevents wound scarring, Appl. Mater. Today 32 (2023) 101785, https://doi.org/10.1016/j.apmt.2023.101785.

[47] H. Miyoshi, T. Adachi, Topography design concept of a tissue engineering scaffold for controlling cell function and fate through actin cytoskeletal modulation, Tissue Eng., Part B 20 (6) (2014) 609–627, https://doi.org/10.1089/ten.teb.2013.0728.

[48] T. Klein, R. Bischoff, Physiology and pathophysiology of matrix metalloproteases, Amino Acids 41 (2) (2011) 271–290, https://doi.org/10.1007/s00726-010-0689-x.

[49] H. Shen, L. Cheng, Q. Zheng, W. Liu, Y. Wang, Scavenging of reactive oxygen species can adjust the differentiation of tendon stem cells and progenitor cells and prevent ectopic calcification in tendinopathy, Acta Biomater. 152 (2022) 440–452, https://doi.org/10.1016/j.actbio.2022.09.007.

[50] L. Qi, B.W. Duan, H. Wang, Y.J. Liu, H. Han, M.M. Han, L. Xing, H.L. Jiang, S. J. Pandol, L. Li, Reactive oxygen species-responsive nanoparticles toward extracellular matrix normalization for pancreatic fibrosis regression, Adv. Sci. 11 (19) (2024) e2401254, https://doi.org/10.1002/advs.202401254.

[51] M. Zhang, H. Liu, Q. Cui, P. Han, S. Yang, M. Shi, T. Zhang, Z. Zhang, Z. Li, Tendon stem cell-derived exosomes regulate inflammation and promote the high-quality healing of injured tendon, Stem Cell Res. Ther. 11 (1) (2020) 402, https://doi.org/10.1186/s13287-020-01918-x.

[52] W. Wang, X. Lin, T. Tu, Z. Guo, Z. Song, Y. Jiang, B. Zhou, D. Lei, X. Wang, W. Zhang, G. Zhou, B. Yi, P. Zhang, W. Liu, Mechanical loading on cell-free polymer composite scaffold enhances in situ regeneration of fully functional Achilles tendon in a rabbit model, Biomater. Adv. 163 (2024) 213950, https://doi.org/10.1016/j.bioadv.2024.213950.

[53] H. Tempfer, A. Traweger, Tendon vasculature in health and disease, Front. Physiol. 6 (2015) 330, https://doi.org/10.3389/fphys.2015.00330.

[54] B. Deng, P. Xu, B. Zhang, Q. Luo, G. Song, COX2 enhances neovascularization of inflammatory tenocytes through the HIF-1α/VEGFA/PDGFB pathway, Front. Cell Dev. Biol. 9 (2021) 670406, https://doi.org/10.3389/fcell.2021.670406.

[55] A.R. Tall, L. Yvan-Charvet, Cholesterol, inflammation and innate immunity, Nat. Rev. Immunol. 15 (2) (2015) 104–116, https://doi.org/10.1038/nri3793.

[56] Y. Geng, X. Zhao, J. Xu, X. Zhang, G. Hu, S.C. Fu, K. Dai, X. Chen, Y.S. Patrick, X. Zhang, Overexpression of mechanical sensitive miR-337-3p alleviates ectopic ossification in rat tendinopathy model via targeting IRS1 and Nox4 of tendon-derived stem cells, J. Mol. Cell Biol. 12 (4) (2020) 305–317, https://doi.org/10.1093/jmcb/mjz030.

[57] C. Petibon, M. Malik Ghulam, M. Catala, S. Abou Elela, Regulation of ribosomal protein genes: an ordered anarchy, Wiley Interdiscip Rev RNA 12 (3) (2021) e1632, https://doi.org/10.1002/wrna.1632.

[58] S.R. Pieczenik, J. Neustadt, Mitochondrial dysfunction and molecular pathways of disease, Exp. Mol. Pathol. 83 (1) (2007) 84–92, https://doi.org/10.1016/j.yexmp.2006.09.008.

[59] F. Addevico, S. Svedman, G. Edman, P.W. Ackermann, Pyruvate and lactate as local prognostic biomarkers of patient outcome after achilles tendon rupture, Scand. J. Med. Sci. Sports 29 (10) (2019) 1529–1536, https://doi.org/10.1111/sms.13469.

[60] D. Tibullo, G. Li Volti, C. Giallongo, S. Grasso, D. Tomassoni, C.D. Anfuso, G. Lupo, F. Amenta, R. Avola, V. Bramanti, Biochemical and clinical relevance of alpha lipoic acid: antioxidant and anti-inflammatory activity, molecular pathways and therapeutic potential, Inflamm. Res. 66 (11) (2017) 947–959, https://doi.org/10.1007/s00011-017-1079-6.

[61] V. Thirunavukkarasu, A.T. Nandhini, C.V. Anuradha, Lipoic acid prevents collagen abnormalities in tail tendon of high-fructose-fed rats, Diabetes Obes. Metabol. 7 (3) (2005) 294–297, https://doi.org/10.1111/j.1463-1326.2004.00418.x.

[62] E. O'Dea, A. Hoffmann, NF-κB signaling, Wiley Interdiscip Rev Syst Biol Med 1 (1) (2009) 107–115, https://doi.org/10.1002/wsbm.30.

[63] T. Liu, L.Y. Zhang, D. Joo, S.C. Sun, NF-κB signaling in inflammation, Signal Transduct. Targeted Ther. 2 (2017), https://doi.org/10.1038/sigtrans.2017.23.

[64] K.H.G. Mills, Induction, function and regulation of IL-17-producing T cells, Eur. J. Immunol. 38 (10) (2008) 2636–2649, https://doi.org/10.1002/eji.200838535.

[65] S. Zhang, J. Zhang, J.J. Yu, X.L. Chen, F.Y. Zhang, W. Wei, L.Y. Zhang, W.M. Chen, N.X. Lin, Y. Wu, Hyperforin ameliorates imiquimod-induced psoriasis-like murine skin inflammation by modulating IL-17A-producing γδ T cells, Front. Immunol. 12 (2021) 635076, https://doi.org/10.3389/fimmu.2021.635076.

[66] Y.L. Zheng, G. Song, J.B. Guo, X. Su, Y.M. Chen, Z. Yang, P.J. Chen, X.Q. Wang, Interactions among lncRNA/circRNA, miRNA, and mRNA in musculoskeletal degenerative diseases, Front. Cell Dev. Biol. 9 (2021) 753931, https://doi.org/10.3389/fcell.2021.753931.

[67] X.Y. Li, N. Yang, X.N. Fang, W. Zhang, J.M. Yao, J.L. Xu, K.L. Song, Coaxial electrospun stretchable nanofiber electrode at wide electrochemical voltage, Colloids Surf. A Physicochem. Eng. Asp. 665 (2023) 131204, https://doi.org/10.1016/j.colsurfa.2023.131204.

[68] W.B. Wang, P. Wang, Q.L. Li, W.F. Dai, B.C. Yi, Z. Gao, W. Liu, X.S. Wang, Piezoelectrically-enhanced composite membranes mimicking the tendinous electrical microenvironment for advanced tendon repair, Nano Today 57 (2024) 102381, https://doi.org/10.1016/j.nantod.2024.102381.

[69] Q. Xu, W.F. Dai, P.Z. Li, Q.L. Li, Z. Gao, X.L. Wu, W. Liu, W.B. Wang, Piezoelectric film promotes skin wound healing with enhanced collagen deposition and vessels regeneration via upregulation of PI3K/AKT, Nano Res. 17 (8) (2024) 7461–7478, https://doi.org/10.1007/s12274-024-6717-z.

[70] J.H. Lu, H.Q. Zhao, Z.J. Wang, X.Y. Lin, W.M. Pi, X. Zhang, L.P. Yang, S.C. Yao, Y. Z. Zhang, X.M. Huang, H.M. Lei, P.L. Wang, Glucose epimerization-modulated phytochemicals constructing carrier-free hydrogel for regulation of macrophage phenotype to promote wound healing, Adv. Funct. Mater. 34 (2024) 2314089, https://doi.org/10.1002/adfm.202314089.

[71] N. Menasria, W.S. Hamdi, W. Zaid A H El Roz, A.H.A. Guled, Dakhilalla M.H. Al-Nabet, A. Comparison of BD stem cell enumeration kit on both FACS Canto ™II software with current laboratory ISHAGE protocol stem cell enumeration assay in single platform, Cytotherapy 22 (5) (2020) S63–S64, https://doi.org/10.1016/j.jcyt.2020.03.094. Supplement.

[72] T. Tu, J. Huang, M.M. Lin, Z. Gao, X.L. Wu, W.J. Zhang, G.D. Zhou, W.B. Wang, W. Liu, CUDC-907 reverses pathological phenotype of keloid fibroblasts *in vitro* and *in vivo* via dual inhibition of PI3K/Akt/mTOR signaling and HDAC2, Int. J. Mol. Med. 44 (5) (2019) 1789–1800, https://doi.org/10.3892/ijmm.2019.4348.

[73] G.A.C. Murrell, E.G. Lilly, H. Davies, T.M. Best, R.D. Goldner, A.V. Seaber, The Achilles functional index, J. Orthop. Res. 10 (3) (1992) 398–404, https://doi.org/10.1002/jor.1100100313.